Effect of Latitudinal variations in low-level baroclinicity on eddy life cycles and upper-tropospheric wave-breaking processes.

Gwendal Riviere

Effect of Latitudinal Variations in Low-Level Baroclinicity on Eddy Life Cycles and Upper-Tropospheric Wave-Breaking Processes

GWENDAL RIVIÈRE

CNRM/GAME, Météo-France/CNRS, Toulouse, France

(Manuscript received 8 August 2008, in final form 24 November 2008)

ABSTRACT

An analysis of the potential vorticity gradient and the refractive index in quasigeostrophic (QG) flows on the sphere reveals that the absolute vorticity and the stretching parts have two contradictory effects on the horizontal shape of the baroclinic waves when the full variations of the Coriolis parameter are taken into account in each term. The absolute vorticity effect favors the anticyclonic (southwest–northeast) tilt and anticyclonic wave breaking (AWB) and is stronger in the upper troposphere. In contrast, the stretching effect promotes the cyclonic (northwest–southeast) tilt and cyclonic wave breaking (CWB) and is more efficient at lower levels. A positive eddy feedback acting on the latitudinal variations of the zonal winds is deduced. Because the absolute vorticity and the stretching effects are respectively more and less efficient with increasing latitude, a more northward (southward) jet renders AWB more (less) probable and CWB less (more) probable; the jet is pushed or maintained more northward (southward) by the eddy feedback.

Idealized numerical experiments using two aquaplanet models on the sphere, a three-level QG model, and a 10-level primitive equation (PE) model, confirm our analysis. Two strategies are employed: first, a normal-mode approach for jets centered at different latitudes; second, an analysis of long-term integrations of the models where the temperature is relaxed toward zonally as well as nonzonally uniform restoration-temperature profiles located at different latitudes. The positive eddy feedback is much less visible in the QG model and CWB is very rare because it does not contain the stretching effect (because of the constant Coriolis parameter in the stretching term).

1. Introduction

Storm tracks and large-scale flow variabilities are closely linked in midlatitudes and their mutual interaction has been the focus of intense research during the last decades. Synoptic weather systems that form the so-called storm tracks take their origin in regions of strong thermal contrasts on the western side of oceanic basins via baroclinic interaction (Hoskins and Valdes 1990). As they reach their maximum amplitude on the eastern side, they feed back onto the large-scale circulation and modify the large-scale winds through the divergence of their momentum fluxes (Hoskins et al. 1983). In the early 1990s, storm tracks have been shown to participate in the maintenance of large-scale flow anomalies (Vautard and Legras 1988; Branstator 1995); very recently, however, several studies have proved that synoptic eddies take an essential part in the formation of these anomalies themselves through wave-breaking processes (Benedict et al. 2004; Rivière and Orlanski 2007; Martius et al. 2007; Strong and Magnusdottir 2008; Woollings et al. 2008). Wave breaking is an asymmetric phenomenon that may modify the large-scale flow anomalies and not necessarily maintain them as they are. The latter works have presented evidences using reanalysis data of the close link between the different kinds of wave breaking and the different phases of the North Atlantic Oscillation (NAO). However, other local teleconnections such as the Pacific–North American pattern are related to wave breaking, too (Orlanski 2005; Martius et al. 2007), as are hemispheric variations of the large-scale flow such as those diagnosed by the zonal index (e.g., Akahori and Yoden 1997) or the annular modes (Vallis and Gerber 2008).

All the large-scale flow variabilities are usually related to variations in position and amplitude of the upper-tropospheric jets (Vallis and Gerber 2008). It can be easily explained why baroclinic waves are able to move

Corresponding author address: Gwendal Rivière, Météo-France, CNRM/GMAP/RECYF, 42 av. G. Coriolis, Toulouse 31057, CEDEX 1, France.
E-mail: gwendal.riviere@meteo.fr

DOI: 10.1175/2008JAS2919.1

the large-scale jets during their breaking. To simplify, there exist two kinds of wave breaking (Thorncroft et al. 1993): anticyclonic wave breaking (AWB) or LC1 and cyclonic wave breaking (CWB) or LC2. If AWB (CWB) occurs around the jet core, it leads to divergence and convergence of momentum fluxes north (south) and south (north) of the jet core, respectively, thus pushing the jet poleward (equatorward). Considering the NAO, it is essentially characterized by wobbling of the upper-tropospheric Atlantic jet between a more northward position (the positive phase) and a more southward position (the negative phase). Despite some nuances among the previously named studies on the NAO, they show that during the formation of its positive and negative phases, AWB and CWB events are respectively more frequent than usual. Following the previous reasoning, wave breaking can be understood as the cause of the jet displacements and the formation of the different phases. But it is not obvious that it cannot also be a consequence since the two phenomena are closely related. The latter aspect will be investigated in the present paper.

To better understand the interaction between the storm tracks and the low-frequency anomalies, it seems crucial to identify factors influencing the different kinds of wave breaking. First of all, geometries affect strongly the main orientation of the eddy momentum fluxes and the nature of the wave breaking, as shown by Balasubramanian and Garner (1997). Momentum fluxes are essentially poleward and AWB dominates in spherical geometry, whereas they are more equatorward in Cartesian geometry and CWB is more present. However, on the sphere, CWB may also happen if the barotropic shear of the jet has a strong cyclonic component, as was initially shown in the idealized simulations of Thorncroft et al. (1993). A transition from AWB to CWB may happen by increasing the amplitude of the cyclonic barotropic shear (see also Hartmann and Zuercher 1998). Similar transitions are possible by modifying other parameters of the environment in which baroclinic waves are embedded, such as the cross-jet asymmetries (Nakamura and Plumb 1994), the strength of the low-level baroclinicity (Orlanski 2003), the vertical shear in the lower stratosphere (Wittman et al. 2007), or the surface friction (Chen et al. 2007). The last two papers show respectively that the increase of the stratospheric shear and the decrease of the surface friction increase the phase speed of the baroclinic waves and lead to more AWB, thus resulting in a poleward shift of the upper jet. Orlanski (2003) found a transition from AWB to CWB in a shallow-water model by increasing the amplitude of the eddy forcing that mimics the increase of the low-level baroclinicity. A nonlinear mechanism based on the asymmetry between cyclones and anticyclones is provided in the latter study in contrast with other ones that usually use linear arguments. Finally, it should be noted that such transitions occur usually for intermediate zonal wavenumbers as 6 or 7 but not for all wavenumbers (see, e.g., Hartmann and Zuercher 1998; Wittman et al. 2007). Wavenumbers above 8 usually break cyclonically and wavenumbers below 5 anticyclonically. For these particularly high and low wavenumbers it was found difficult by the different authors to get the reverse wave breaking.

The aim of the present paper is to investigate the effect of the jet latitude on eddy life cycles and wave breaking processes. Simmons and Hoskins (1978) have already looked at the impact of different kind of jets located at different latitudes on the nonlinear stages of baroclinic eddy life cycles, but not systematically and not in terms of wave breaking. Furthermore, their study was only based on the life cycles of normal modes, whereas the present work will lean on normal-mode analysis as well as forced long-term simulations. The essential motivation is to clarify the eddy feedback onto large-scale flow anomalies such as the NAO or the annular modes. Because most of these large-scale flow anomalies are characterized by wobbling of the upper-tropospheric jet between different latitudinal positions, it is important to understand the impact of the jet latitude on wave breaking. As already said, there exists a close relationship in reanalysis data and GCM simulations between AWB and more northward positions of the jet and between CWB and more southward positions, but these two phenomena are interwoven. To separate the problem, we impose in our idealized experiments some latitudinal positions for the jet or the low-level baroclinicity and analyze their effect on eddy life cycles.

The paper is organized as follows: Two dry aquaplanet models on the sphere are used in the study and presented in section 2; one is under the quasigeostrophic framework and the other is a simplified global atmospheric primitive equation model. Section 3 presents two competing effects determining the horizontal tilt of the eddies in terms of potential vorticity (PV) gradients and refractive index. It provides a rationale for the jet-latitude effect on the shape of the baroclinic waves and their breaking. Section 4 consists of a normal-mode study. Long-term simulations of the two models using different restoration-temperature profiles located at different latitudes are interpreted in section 5. Finally, conclusions are presented in section 6.

2. Models

a. Quasigeostrophic model

The first model used in this study is the quasigeostrophic (QG) model of Marshall and Molteni (1993,

hereafter MM93). It is a three-level spectral model on the sphere that integrates the PV equation at each vertical level i:

$$\frac{\partial q_i}{\partial t} = -J(\psi_i, q_i) - D_i(\psi_1, \psi_2, \psi_3) + S_i, \quad (1)$$

where q_i and ψ_i denote the PV and the streamfunction. Levels 1, 2, and 3 correspond respectively to 200, 500, and 800 hPa. PV is defined as

$$q_1 = f + \nabla^2\psi_1 - R_{01}^{-2}(\psi_1 - \psi_2), \quad (2)$$

$$q_2 = f + \nabla^2\psi_2 + R_{01}^{-2}(\psi_1 - \psi_2) - R_{02}^{-2}(\psi_2 - \psi_3), \quad (3)$$

$$q_3 = f + \nabla^2\psi_3 + R_{02}^{-2}(\psi_2 - \psi_3), \quad (4)$$

where $f = 2\Omega\sin\varphi$ is the Coriolis parameter; $R_{01} = 660$ km and $R_{02} = 400$ km are Rossby radii of deformation for the 200–500- and 500–800-hPa layers, respectively, and are slightly weaker than in MM93 to get stronger and more realistic storm tracks. A T42 version is used without topography but all the results can be recovered using a T21 truncation. Each term $D_i(\psi_1, \psi_2, \psi_3)$ is the sum of linear operators including a Newtonian relaxation of temperature, a linear drag at the surface (for $i = 3$), and a horizontal diffusion. For the normal-mode study (section 4), D_i has the same expression as in MM93 and S_i is zero, whereas for the forced simulations (section 5), a constant S_i corresponding to the restoration-temperature profile is added (see appendix A for an exact formulation).

b. Primitive equation model

The second model is the simplified global atmospheric circulation model known as the Portable University Model of the Atmosphere (PUMA; Fraedrich et al. 2005; http://www.mi.uni-hamburg.de/Downloads.245.0.html). It is a primitive equation spectral model on the sphere with ten equally spaced sigma levels in the vertical. A T42 truncation is used in most parts of the study unless the text explicitly says otherwise. Orography and moisture are not included. Rayleigh friction is applied to the two lowest levels with a time scale of about 1 day at $\sigma = 0.9$. Hyperdiffusion has a damping time scale of 0.1 days. In section 5, a Newtonian relaxation to a prescribed temperature field is added to the model, similarly to what was done in Frisius et al. (1998, hereafter FR98).

3. Two competing effects acting on wave breaking

The aim of this section is to present two competing asymmetric effects included in the basic-state PV gradient that act differently on the horizontal shape of the baroclinic waves and their breaking. Considering a zonal jet with a symmetric profile centered at latitude φ_0, the corresponding PV gradient can be asymmetric, which may lead to asymmetric eddy momentum fluxes as already noticed by Nakamura (1993). To analyze this aspect, we introduce the refractive index in quasigeostrophic flows [developed by Matsuno (1970)] and where the PV gradient plays a crucial role. It is only valid for linear wave dynamics but has been shown to be useful for interpreting wave breaking processes (see, e.g., Thorncroft et al. 1993; Lee and Feldstein 1996) and takes the following form:

$$n^2 = \left(\frac{\partial\overline{q}/\partial y}{\overline{u} - ca\cos\varphi} - \frac{f^2}{4H^2N^2} - \frac{m^2}{a^2\cos^2\varphi}\right)\Big/\sin^2\varphi, \quad (5)$$

where $\overline{u}$ and $\overline{q}$ are respectively the basic-state zonal wind and PV, c is the angular velocity of the disturbance, a the earth's radius, N the Brunt–Väisälä frequency, H the scale height, and m the zonal wavenumber. The PV gradient in pressure coordinates can be written as

$$\frac{\partial\overline{q}}{\partial y} = \frac{2\Omega\cos\varphi}{a} + \frac{1}{a}\frac{\partial\overline{\zeta}}{\partial\varphi} - f^2\frac{\partial}{\partial p}\left[\left(\frac{\rho g}{N}\right)^2\frac{\partial\overline{u}}{\partial p}\right], \quad (6)$$

where $\overline{\zeta}$ is the basic-state relative vorticity, ρ is the density, g is the gravitational acceleration, and p is the pressure. Interpretation of the refractive index is as follows: In regions where n^2 is positive, waves propagate, whereas in regions where n^2 is negative, they are evanescent. Furthermore, in regions of propagation, waves tend to be refracted toward larger n^2. In a barotropic context where the PV gradient is reduced to the absolute vorticity gradient [first two terms on the right-hand side of (6)], the largest values of n^2 are located more on the south side of the jet because of metric terms and the y derivative of f. This asymmetry of the effective beta is a classical argument to explain why midlatitude waves are essentially refracted toward subtropics and get a dominant southwest (SW)–northeast (NE) tilt (e.g., James 1994; Orlanski 2003). However, in a baroclinic context, the variations of f also appear in the stretching term [third term on the right-hand side of (6)] and have an opposite effect. Indeed, in the upper troposphere, this term is positive and stronger in the north than in the south. There is thus a competition between the absolute vorticity and the stretching parts of the PV gradient.

To get a quantitative estimation of the PV gradient for realistic values, we use the formulation of the three-layer QG model described in section 2. Because the model contains constant Rossby radii of deformation, the underlying f in the stretching term is reduced to a

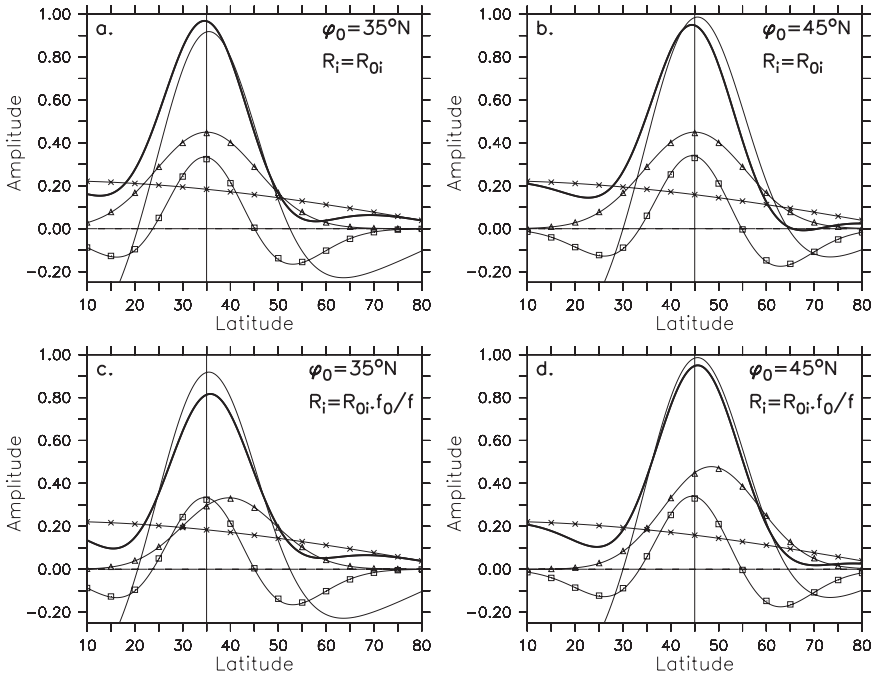

FIG. 1. The meridional PV gradient at 200 hPa divided by a constant value 6.5×10^{-4} m^{-1} s^{-1} (heavy solid line) as the sum of the stretching term (solid line with triangles) and the y derivatives of the relative vorticity (solid line with squares) and of the Coriolis parameter (solid line with crosses); $u - ca\cos\varphi$ divided by a constant value 32 m s^{-1} is represented by the solid line, and the vertical line marks φ_0. (a) $R_i = R_{0i}$, $\varphi_0 = 35°$N, (b) $R_i = R_{0i}$, $\varphi_0 = 45°$N, (c) $R_i = R_{0i} f_0/f$, $\varphi_0 = 35°$N, and (d) $R_i = R_{0i} f_0/f$, $\varphi_0 = 45°$N. The angular velocity is $c = 3 \times 10^{-6}$ s^{-1}.

constant f_0 whereas its full variations are taken into account in the absolute vorticity [see Eq. (2)]. This simplification is needed to get a consistent QG model on the sphere [as described in appendix A of MM93 or in more detail by Mak (1991)]. But because our goal is to quantify the different terms of Eq. (6) with their complete expression, we define new Rossby radii of deformation that may vary with latitude. The basic-state PV gradients are expressed as

$$\overline{q}_{1y} = \frac{2\Omega\cos\varphi}{a} + \frac{1}{a}\frac{\partial\overline{\zeta}_1}{\partial\varphi} + R_1^{-2}(\overline{u}_1 - \overline{u}_2), \tag{7}$$

$$\overline{q}_{2y} = \frac{2\Omega\cos\varphi}{a} + \frac{1}{a}\frac{\partial\overline{\zeta}_2}{\partial\varphi} - R_1^{-2}(\overline{u}_1 - \overline{u}_2) + R_2^{-2}(\overline{u}_2 - \overline{u}_3), \tag{8}$$

$$\overline{q}_{3y} = \frac{2\Omega\cos\varphi}{a} + \frac{1}{a}\frac{\partial\overline{\zeta}_3}{\partial\varphi} - R_2^{-2}(\overline{u}_2 - \overline{u}_3). \tag{9}$$

If $R_i \equiv R_{0i}$, the estimation of the basic-state PV gradient is exactly that of the QG model. If $R_i \equiv R_{0i} f_0/f$ where f_0 is the value of f at latitude 45°N, the stretching term is proportional to f^2 as in the more general expression of Eq. (6). The PV gradients of Figs. 1 and 2 are obtained by defining a zonal jet with a symmetric Gaussian profile of standard deviation 15°.

Let us first describe the PV gradient at the upper level for constant R_i (Figs. 1a,b). Although the zonal wind is symmetric, the relative vorticity gradient is asymmetric because of the metric terms and reaches slightly greater values on the south side of the jet than on the north side (e.g., compare the slight difference between the two minima on both sides of the jet). Because the derivative of f decreases with latitude, the two terms implied in the absolute vorticity gradient have the same effect and make the PV gradient at the upper level stronger south of the jet. The asymmetry between the two sides of the jet is more visible for the 45° jet (Fig. 1b) than the 35° jet (Fig. 1a), as can be seen by comparing the two minima of the PV gradient on both sides of the jet. The minima on the south side have almost the same value, but on the north side the minimum in Fig. 1b is almost zero (at 65°N) whereas it is positive in Fig. 1a (at 55°N). Even though this difference is slight, it appears close to the zero of $\overline{u} - ca\cos\varphi$ and has a non-negligible impact when the PV gradient is divided by $\overline{u} - ca\cos\varphi$ to get the refractive index (see discussion of Fig. 3). This jet-latitude effect is logical because $\cos\varphi$ (which intervenes

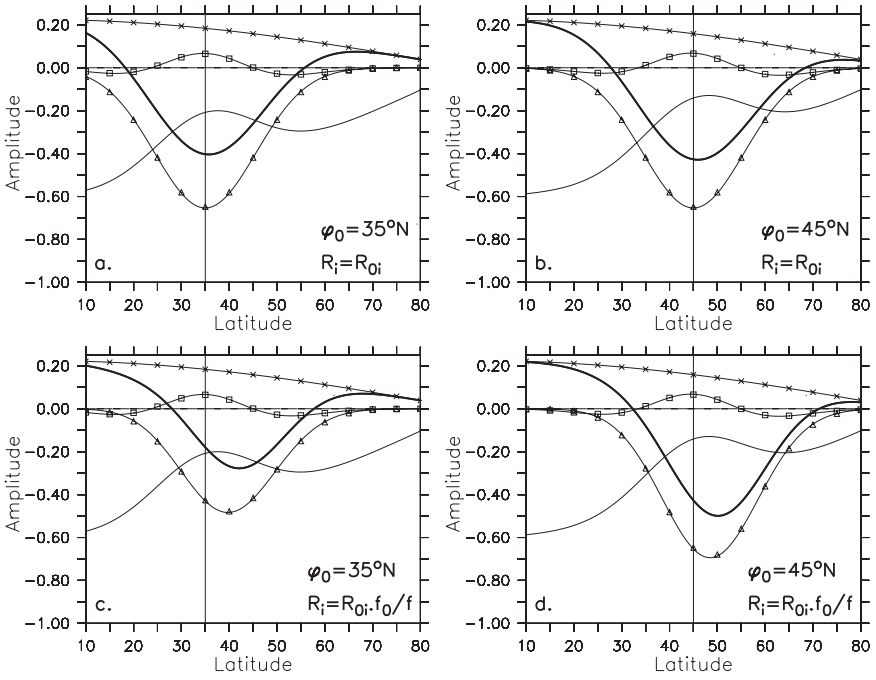

FIG. 2. As in Fig. 1, but at 800 hPa.

in the gradient of f) has larger variations in high latitudes than in low latitudes.

For latitude-varying R_i (Figs. 1c,d), the stretching gradient is no longer symmetric and is greater on the north side of the jet. It has the opposite effect of the absolute vorticity gradient and compensates it in part. For example, the minimum located on the south side decreases whereas that on the north side increases from Fig. 1a to Fig. 1c or from Fig. 1b to Fig. 1d. The PV gradient has still slightly stronger values south of the jet core in Fig. 1d but is less asymmetric than in Fig. 1b. In Fig. 1c, the PV gradient is even closer to a symmetric shape. To conclude, the most asymmetric PV gradients are obtained for jets located at higher latitudes and for constant R_i (i.e., in Fig. 1b). This asymmetry favors stronger refractive index on the south side making the waves tilt anticyclonically (SW–NE).

The PV gradient at 800 hPa is shown in Fig. 2. At this level, the refractive index has positive values in regions of negative PV gradient due to the negative values of $u - ca\cos\varphi$. For constant R_i (Figs. 2a,b), the PV gradient minimum is reached about the jet core with slightly larger negative values on the north side because of the slight asymmetric absolute vorticity gradient. By considering latitude-varying R_i (Figs. 2c,d), the minimum of the PV gradient is shifted 5° northward because of the strong negative stretching term on the north side of the jet. At 800 hPa, the PV gradient reaches strong negative values north of the jet essentially because of the stretching gradient and slightly because of the absolute vorticity gradient.

An intermediate computation of the refractive index is shown in Fig. 3; it is obtained by replacing φ by the constant φ_0 in all terms of Eq. (5) apart from the first term to look first at the PV gradient impact. At the upper level, the intermediate refractive index reaches stronger values south of the jet in Figs. 3a,b,d with a more pronounced asymmetry in Fig. 3b, whereas it is more or less symmetric in Fig. 3c. This reflects the shapes of the PV gradient and $\overline{u} - ca\cos\varphi$ shown in Fig. 1. At the lower level, the intermediate refractive index is slightly greater north of the jet in Figs. 3a,b, but the asymmetry is much stronger in Figs. 3c,d because of the asymmetry of the stretching term discussed in Fig. 2. The total refractive index is close to the intermediate one with just a systematic bias toward larger values south of the jet, essentially because of the variations of φ in the third term of Eq. (5). At the upper level, n^2 has strong positive values south of the jet for all four panels of Fig. 3. This asymmetry is stronger for the 45° jet where negative values of n^2 are reached north of the jet (Figs. 3b,d). In contrast, n^2 is positive north of the 35° jets, with a minimum close to zero in Fig. 3a and a positive minimum in Fig. 3c. The refractive index is therefore less asymmetric for lower-latitude jets and latitude-varying R_i (Fig. 3c). Because waves tend to be refracted toward larger n^2 that are more southward at the upper level, their propagation will be mainly equatorward, getting a dominant SW–NE

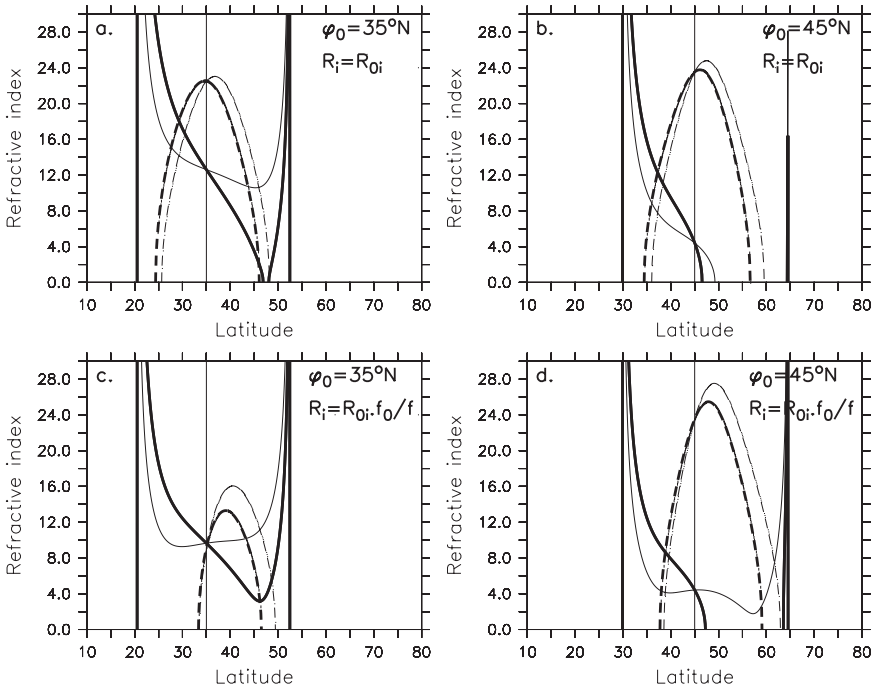

FIG. 3. Refractive index defined as $a|n|\text{sign}(n^2)$ (nondimensional values) at 200 hPa (thick solid lines) and at 800 hPa (thick dashed lines) for (a) $R_i = R_{0i}$, $\varphi_0 = 35°$N, (b) $R_i = R_{0i}$, $\varphi_0 = 45°$N, (c) $R_i = R_{0i}f_0/f$, $\varphi_0 = 35°$N, and (d) $R_i = R_{0i}f_0/f$, $\varphi_0 = 45°$N. The thin lines correspond to the refractive index when φ is replaced by φ_0 in all terms of Eq. (5) apart from the first term, where the full variations of φ are kept. All n^2 are computed for $m = 7$, $c = 3 \times 10^{-6}$ s^{-1}, $H = 8000$ m, and $N = 0.01$ s^{-1}. Other values are given in the text.

tilt. Because the refractive index theory is strictly valid for normal-mode analysis and because normal modes do not change their structure with time, we expect to see a dominant SW–NE tilt in their horizontal shape at this level. It is only in the case of lower-latitude jets that the reverse tilt may eventually appear. However, n^2 at the lower level is different. It has a quite symmetric shape in Figs. 3a,b with a positive maximum around the jet core, but it is asymmetric when R_i varies with latitude with a maximum shifted few degrees northward of the jet core in Figs. 3c,d, which may lead to a predominance of the cyclonic [northwest (NW)–southeast (SE)] tilt at this level. This displacement due to the stretching term is slightly stronger for the 35° jet than for the 45° jet because f varies more rapidly at lower latitudes than at higher ones.

In conclusion, when the full variations of f are taken into account in each term, the absolute vorticity gradient and the stretching gradient have opposite effects (hereafter called the absolute vorticity effect and stretching effect). The absolute vorticity effect favors the anticyclonic tilt at upper levels; however, the stretching effect compensates in part the previous effect at upper levels and may lead to the cyclonic tilt at lower levels. Because the dominant tilt of the waves is closely related to the kind of wave breaking, it suggests that AWB and CWB are promoted by the absolute vorticity gradient and the stretching gradient, respectively. Note that because the QG model does not include the variations of f in the stretching term, CWB should be rare in this model.

The stretching effect can be also deduced from the thermal wind relation

$$p\frac{\partial u}{\partial p} = \frac{R}{f}\frac{\partial T}{\partial y}, \tag{10}$$

where R is the gas constant for dry air and T is temperature. The factor f^{-1} (i.e., $\sin^{-1}\varphi$) in (10) shifts the maximum vertical wind shear equatorward of the region of maximum temperature gradient. The maximum zonal wind is thus generally located south of the maximum baroclinicity. Eddies growing in regions of strong baroclinicity are embedded in an environment where the horizontal shear is cyclonic; they therefore tend to tilt cyclonically.

The impact of the jet latitude is easily interpreted from the two competing effects. With the latitudinal variations of the absolute vorticity gradient and of the stretching gradient increasing and decreasing respectively with latitude, the cyclonic tilt and CWB are favored for low-latitude jets and the anticyclonic tilt and AWB for high-latitude ones. The two effects therefore play a

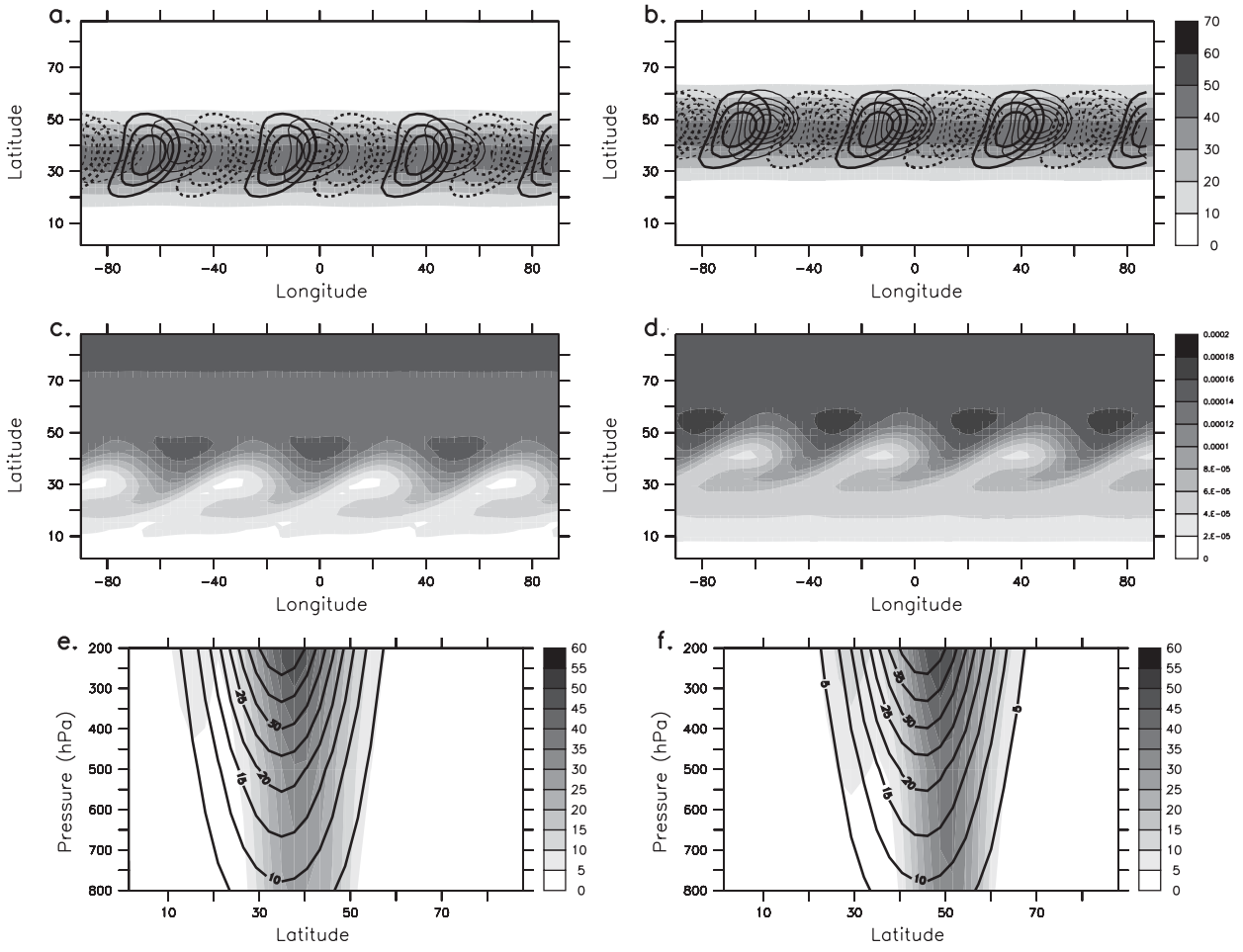

FIG. 4. Normal-mode structure and evolution using the QG model for a wavenumber-7 disturbance embedded in a (left) 35° and (right) 45° jet. (a),(b) Basic-state zonal winds (shading; interval: 10 m s^{-1}) and normal-mode meridional velocities at 200 hPa (heavy contours) and 800 hPa (light contours) normalized by the maximum at the upper level (interval: 0.2). (c),(d) Absolute vorticity after 6 days (interval: 2×10^{-5} s^{-1}). (e),(f) Meridional cross sections of zonally averaged zonal winds at the initial time (black contours) and after 10 days (shading; interval: 5 m s^{-1}).

constructive role. Because the QG model contains only the absolute vorticity effect but the PE model has both effects, we expect the jet-latitude effect to be more visible in the latter.

4. Normal-mode study

The initial structures of normal modes and their nonlinear evolution are now investigated in the QG and PE models for basic-state zonal winds having the same symmetric Gaussian profile but differing in their latitudinal position.

a. QG model

Figure 4 compares the structure and the evolution of two normal modes corresponding to a 35° jet (left column) and a 45° jet (right column) for zonal wavenumber 7. The structure of each normal mode is more or less symmetric at the lower level whereas a clear anticyclonic tilt appears at the upper level for both modes, consistent with the stronger efficiency of the absolute vorticity effect at upper levels. Furthermore, the anticyclonic tilt is more pronounced for the 45° jet than the 35° jet as expected. Their nonlinear evolution is characterized by a strong AWB (Figs. 4c,d) and leads to a poleward shift of both jets after 10 days (Figs. 4e,f). Because the difference between these two evolutions is quite slight, the same analysis was made for a 30° jet (Fig. 5). The normal mode at the upper level (Fig. 5a) is less asymmetric than the previous two modes. Its nonlinear evolution is still essentially characterized by AWB, but one contour of absolute vorticity presents a CWB signature north of the jet (Fig. 5b), which was not the case in Figs. 4c,d. As the jet latitude decreases, there

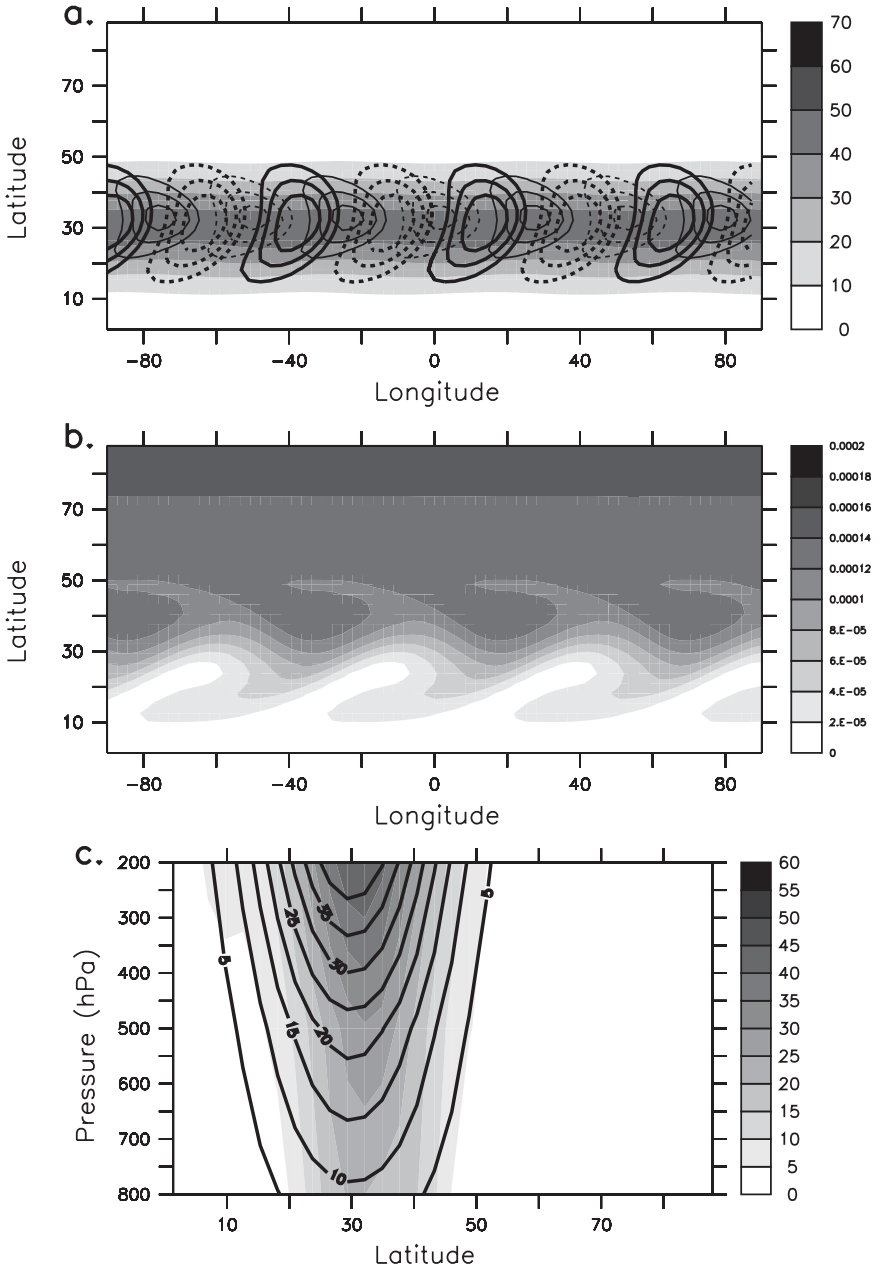

FIG. 5. As in the left column of Fig. 4, but for a 30° jet.

is a continuous evolution of the corresponding normal mode toward a more symmetric structure, a less obvious AWB, and a less pronounced poleward shift of the jet (see Fig. 5c).

The growth rates for different wavenumbers are shown in Fig. 6a. The most unstable wavenumbers are 8, 9, and 10 for the 35° jet and 6, 7, and 8 for the 45° jet (Fig. 6a). As a given wavenumber does not correspond to the same wavelength for the two jets, growth rates are plotted as function of wavelength in Fig. 6b. The most unstable wavelength is slightly smaller for the 35° jet than for the 45° jet, and growth rates for wavelengths larger than 5000 km are significantly greater for the 45° jet. The evolutions of the zonally averaged zonal winds after 10 days are shown in Fig. 7 for different wavenumbers. All normal modes during their decay stage push the jet poleward, and some of them also accelerate it. The most efficient wavenumbers in shifting the jet are generally the most unstable ones: wavenumbers 7, 8, and 9 for the 35° jet (Fig. 7a) and 6, 7 and 8 for the 45° jet

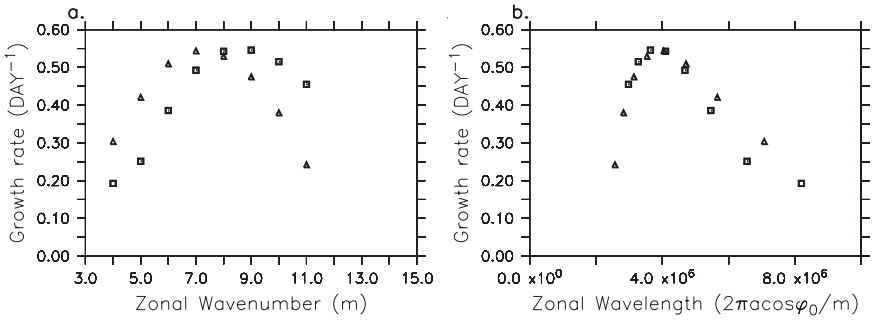

FIG. 6. Normal-mode growth rates using the QG model as function of (a) zonal wavenumber and (b) zonal wavelength for the 35° (squares) and 45° jet (triangle).

(Fig. 7b). However, a bias toward large spatial scales exists; for example, for the 45° jet, wavenumber 10 modifies the jet less strongly than wavenumber 5, although they have almost the same growth rate (0.4 day^{-1}). The same result can be seen in Fig. 7a for the 35° jet by comparing wavenumbers 7 and 10. In other words, normal modes with large wavelengths are more able to move the jet poleward and to accelerate it than small wavelengths with equivalent growth rates. To conclude, as the jet latitude increases, synoptic waves become more efficient at pushing the jet poleward not only because of the absolute vorticity effect and the more pronounced AWB feature for a given wavelength but also because the jet-latitude increase acts to augment the growth rates of larger waves, which have usually more impact on the jet during their AWB.

b. PE model

A similar normal-mode analysis was performed using the PE model. The normal-mode horizontal shapes in Figs. 8a,b are quite different from those in Figs. 4a,b. At the upper level, the SW–NE tilt is less obvious; at the lower level, there is a clear NW–SE tilt appearing in Figs. 8a,b that is not present in Figs. 4a,b. It is consistent with the refractive index and the presence of the stretching effect in the PE model only. The SW–NE tilt at the upper level is hardly visible in the more southward jet and the NW–SE tilt at the lower level is stronger for the 35° jet than for the 45° jet. The decrease of the jet latitude accentuates the cyclonic tilt at the lower level and reduces the anticyclonic tilt at the upper level. This difference in the initial shape of the two normal modes provides a qualitative explanation of the large difference of behavior during their nonlinear stage (Figs. 8c,d). Wave breaking in both cases is not purely CWB or AWB, but the AWB signature clearly dominates for the 45° jet and CWB is more present for the 35° jet. The upper-level jet after 10 days is north of its initial position in both cases but the northward displacement is stronger for the 45° jet. The low-level westerlies are also displaced poleward in the high-latitude case, whereas they do not move in the low-latitude case (see Figs. 8e,f).

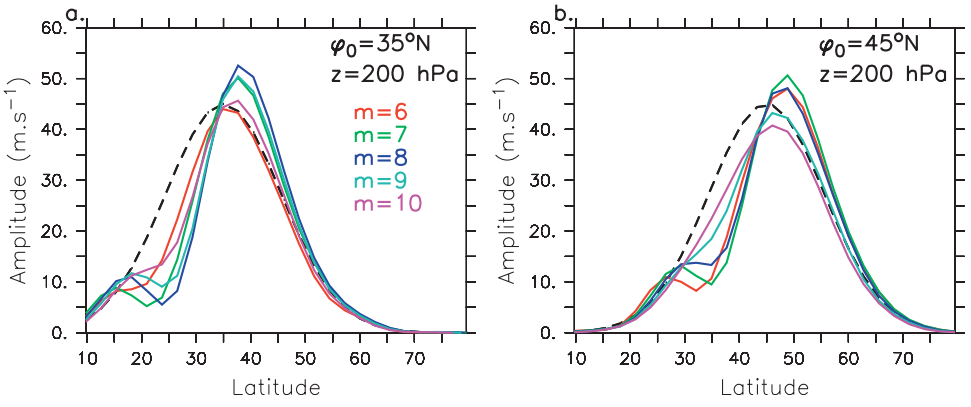

FIG. 7. Zonally averaged zonal winds at 200 hPa after 10 days as function of zonal wavenumber using the QG model for the (a) 35° and (b) 45° jets. Zonal winds corresponding to wavenumbers 6, 7, 8, 9, and 10 are respectively represented by the lines in red, green, blue, light blue, and magenta. The zonal wind at the initial time is represented by the black dashed line.

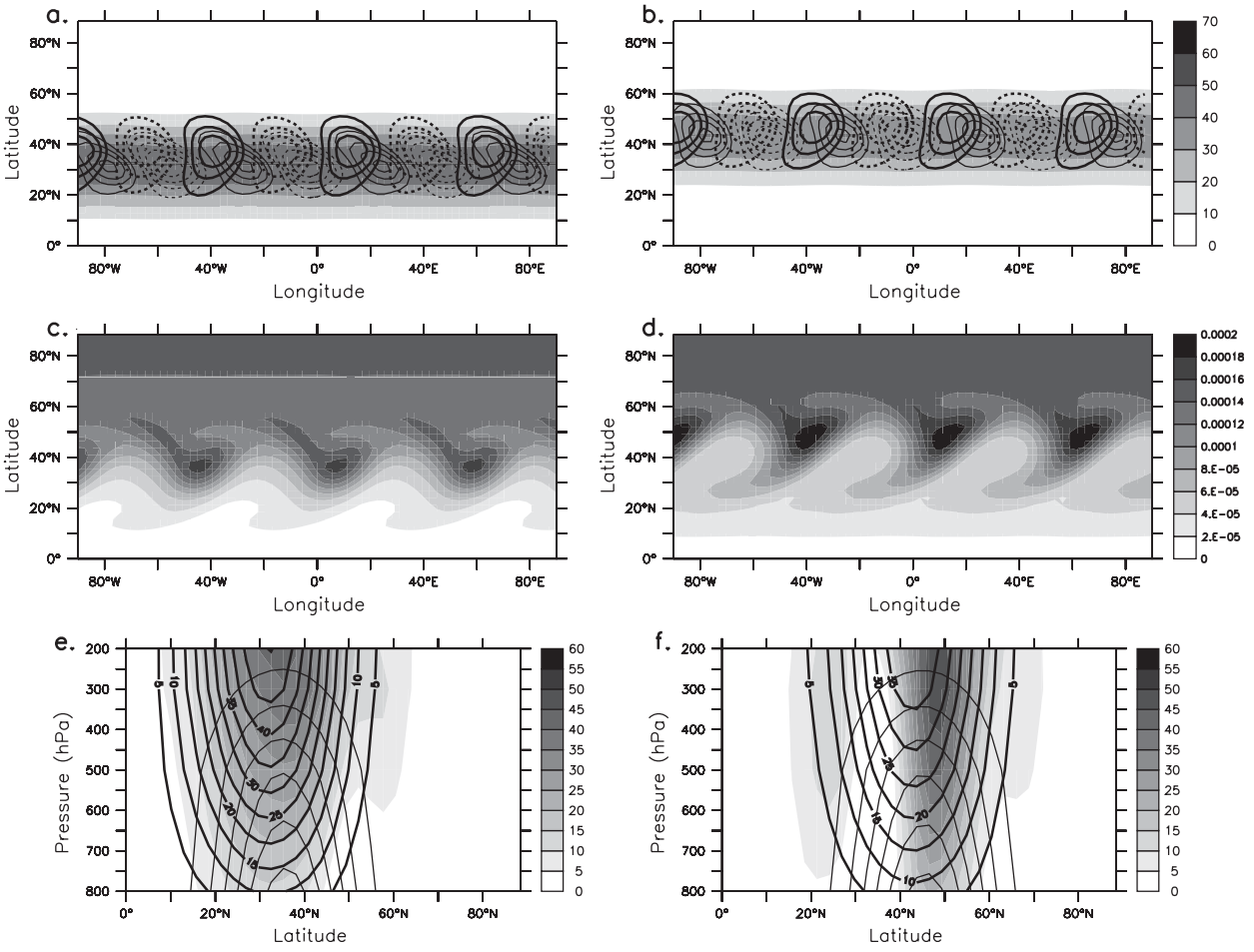

FIG. 8. As in Fig. 4, but using the PE model. The light contours (interval: 10^{-5} s^{-1}) in (e) and (f) correspond to the baroclinicity centered at 35° and 45°N, respectively.

The normal mode for wavenumber 8 (Fig. 9) is more confined meridionally than for wavenumber 7, especially at the upper level. Indeed, as wavenumber increases, regions of wave propagation are thinner according to the refractive index theory [see the third term on the right-hand side of Eq. (5)] and the mode has thus a thinner meridional extent. Another difference is that the mode at wavenumber 8 has a stronger amplitude at low levels compared to that at wavenumber 7. We have noticed the general property that modes for high wavenumbers are much more localized at low levels than those for low wavenumbers. This may explain why high wavenumbers tend to break more cyclonically; the stretching and absolute vorticity effects are respectively more and less efficient at low levels. There is no drastic change from wavenumbers 7 to 8 but an evolution toward less AWB and more CWB is perceptible. Indeed, the absolute vorticity contour 2.10^{-5} s^{-1} in Fig. 8c exhibits an anticyclonic reversal of the gradient, whereas no such reversal appears for the same contour in Fig. 10c. Similarly, two contours have an anticyclonic signature in Fig. 8d but only one in Fig. 10d. The AWB signal is therefore less important in Figs. 10c,d than in Figs. 8c,d. This difference between wavenumbers 7 and 8 is confirmed by the eddy momentum fluxes; the amplitude of the negative momentum fluxes are almost the same for the two wavenumbers whereas the positive momentum fluxes are systematically much weaker for wavenumber 8 than for wavenumber 7 (e.g., cf. Figs. 10a and 11a). At wavenumber 8, pure CWB appears for the 35° jet and a mix of AWB and CWB for the 45° jet. The difference of impact on the zonal winds after 10 days is spectacular, with a southward shift of the jet for the former case (Fig. 9e) and a northward shift for the latter (Fig. 9f).

Growth rates for different wavenumbers are shown in Fig. 12. The most unstable wavelengths are quite similar for the two jets (Fig. 12b), in contrast with the QG model. The impact on the jet evolution varies: for the 45° jet, all wavenumbers between 6 and 8 push the

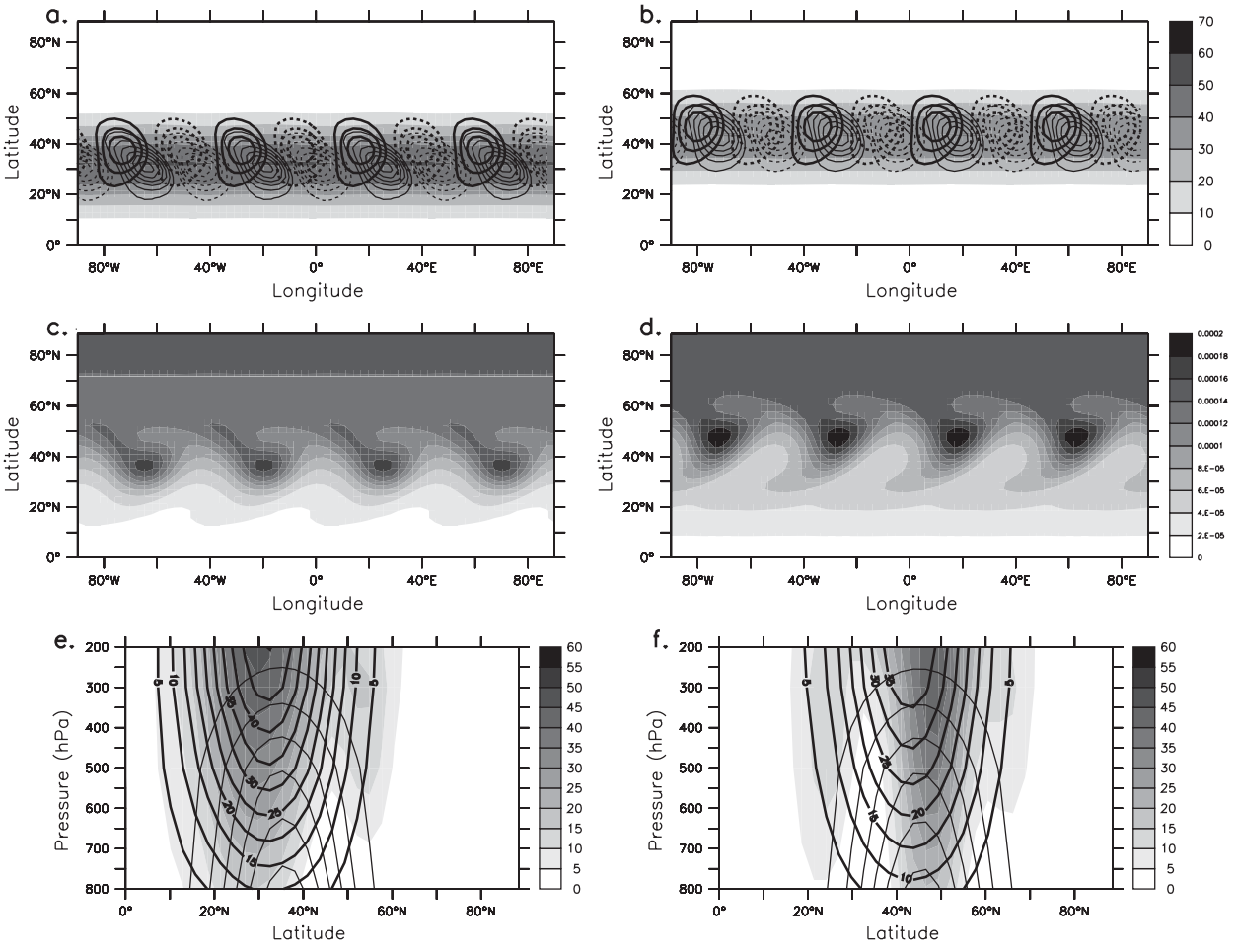

FIG. 9. As in Fig. 8, but for wavenumber 8.

upper-level jet poleward and accelerate it, wavenumber 9 reduces its amplitude without modifying its position, and wavenumber 10 displaces it slightly southward (Fig. 13b). In contrast, for the 35° jet (Fig. 13a), only wavenumber 6 moves the upper-level jet poleward, whereas wavenumbers 8, 9, and 10 move it very slightly southward. It seems difficult to get a frank southward displacement of the upper-level jet even for the strongest CWB events, perhaps because the amplitudes of the waves are concentrated at low levels during such

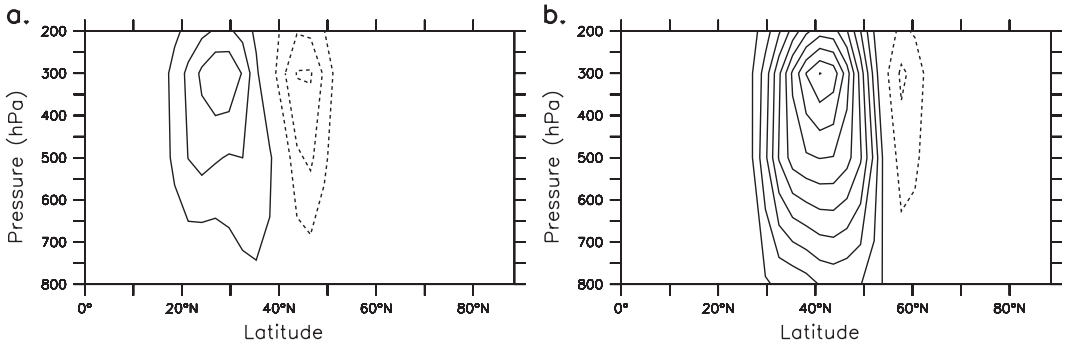

FIG. 10. (a),(b) Zonally averaged eddy momentum fluxes $\overline{u'v'}$ (the overbar denotes here a zonal average and the prime a deviation from the zonal average) for the same simulations and the same time as in Figs. 8c and 8d, respectively (interval: 20 m^2 s^{-2}; solid and dashed lines indicate positive and negative values, respectively).

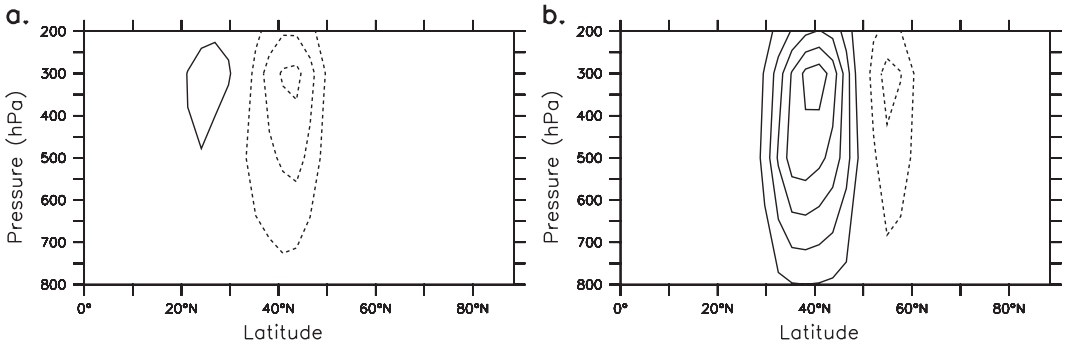

FIG. 11. (a),(b) Zonally averaged eddy momentum fluxes for the same simulations and time as in Figs. 9c and 9d, respectively. Contour interval is as in Fig. 10.

events. For the same reason, the low-level westerlies are significantly pushed southward in Fig. 13c for almost all wavenumbers other than wavenumber 6. For the 45° jet, the low-level westerlies get a more northward position for wavenumbers 6, 7, and 8 and a more southward position for wavenumbers 9 and 10. To summarize, for the 45° jet, most of the wavenumbers displace the low-level westerlies northward and accelerate them, whereas for the 35° jet the low-level westerlies are also accelerated, but in a southward direction.

To conclude this section on normal modes, CWB is almost entirely missing in the nonlinear evolution of the normal modes in the QG model for the different symmetric jets considered. For almost all wavenumbers, the eddy feedback is dominated by AWB, which pushes the jet poleward with slightly more efficiency for the more northward initial jets. It is consistent with the refractive index showing that the SW–NE tilt related to the absolute vorticity effect becomes stronger as the jet latitude increases. However, CWB appears clearly in the evolution of the normal modes of the PE model for very high wavenumbers or for the more southward jet. Wave breaking processes in the PE model are strongly sensitive to the jet latitude. The anticyclonic (cyclonic) tilt appears more easily as the jet latitude increases (decreases), thereby making AWB (CWB) more probable. These results reveal a positive eddy feedback acting on the jet latitude: the more the jet is northward (southward), the more the eddy feedback will tend to push it northward (southward).

5. Long-term simulations

a. Restoration time scales and storm-track climatologies

The aim of the present section is to confirm the positive eddy feedback found in the normal-mode analysis but in the context of long-term simulations using a relaxation toward a prescribed temperature field. In the QG model, the restoration time scale is 25 days between the two upper levels and 5 days between the two lower levels (see appendix A). In the PE model, the time scale is 30 days in the upper levels for $\sigma > 0.35$ and 10 days at $\sigma = 0.7$; it decreases to 2 days at the lowest level ($\sigma = 0.95$). These time scales are similar to those used in equivalent experiments [as, e.g., in FR98 and Gerber and Vallis (2007)].

Each simulation is initialized with a random perturbation and run for two years. The time averages are computed for the last year only. Simulations with longer

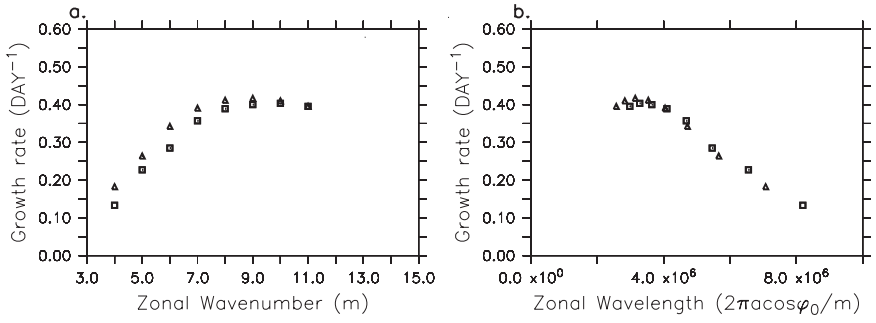

FIG. 12. As in Fig. 6, but using the PE model.

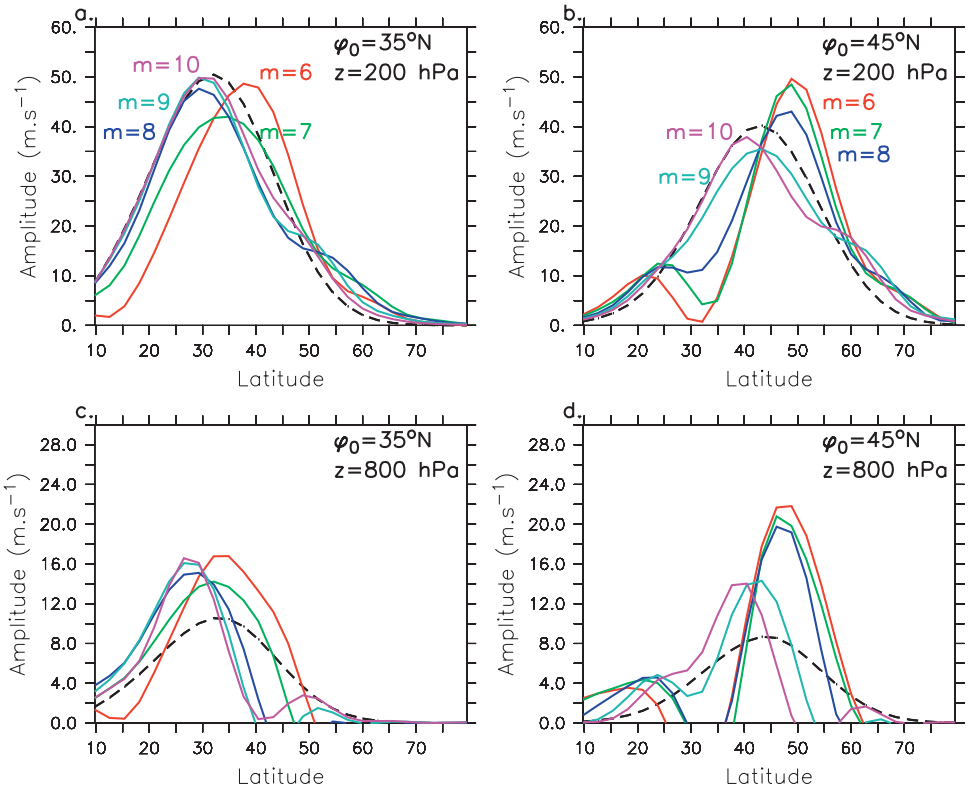

FIG. 13. (a),(b) As in Fig. 7, but using the PE model. (c),(d) As in (a),(b) but at 800 hPa.

periods have been performed (not shown) but do not change the qualitative picture of the climatologies. A daily dataset is extracted from each simulation to which is applied a 15-point Lanczos high-pass filter with a 10-day cutoff to get the high-frequency eddy signal. In what follows, a systematic comparison is made between runs whose restoration-baroclinicity fields ($f/N\partial\overline{u}/\partial z$) have the same shape and amplitude but are centered at different latitudes. To assess the frequency of occurrence of AWB and CWB events in each simulation, a wave-breaking detection method is applied (explained in appendix C). At each time, it systematically detects regions of reversal of the absolute vorticity gradient and discriminates between AWB and CWB.

b. *Relaxation toward zonally uniform temperature field*

1) EXPERIMENTAL DESIGN

In both models, the temperature profile is defined as an erf function whose y derivative takes a Gaussian form. If no perturbation is initially added to start the simulation, then because the forcing is zonally uniform no perturbation develops during the entire simulation and the mean temperature is very close to the restoration temperature. A perturbation is therefore added to the initial state to get nontrivial simulations. We have checked that climatologies do not depend strongly on the shape and the amplitude of the perturbation. However, it will be interesting to see the position of the mean jet with and without an initial perturbation because it will allow us to interpret the eddy feedback onto the large-scale westerlies.

2) RESULTS

Figure 14 compares two simulations of the QG model whose restoration fields differ only in the latitude of the baroclinicity maximum. Whatever the day of the simulations, the absolute vorticity field exhibits strong AWB in both simulations as in Figs. 14a,b. The time-averaged high-frequency momentum fluxes are positive and the high-frequency kinetic energy is concentrated at upper levels in both simulations (Figs. 14e,f). The time-mean jet with perturbation is 10° more northward than the time-mean jet without perturbation, consistent with the strong dominant AWB signal in both cases (Figs. 14c,d). However, the two simulations slightly differ in two aspects. In the low-latitude case, a weak CWB signature is visible, especially at 500 hPa (Fig. 14g), whereas it does not appear in the high-latitude case, which is more characterized by pure AWB events (Fig. 14h). A difference

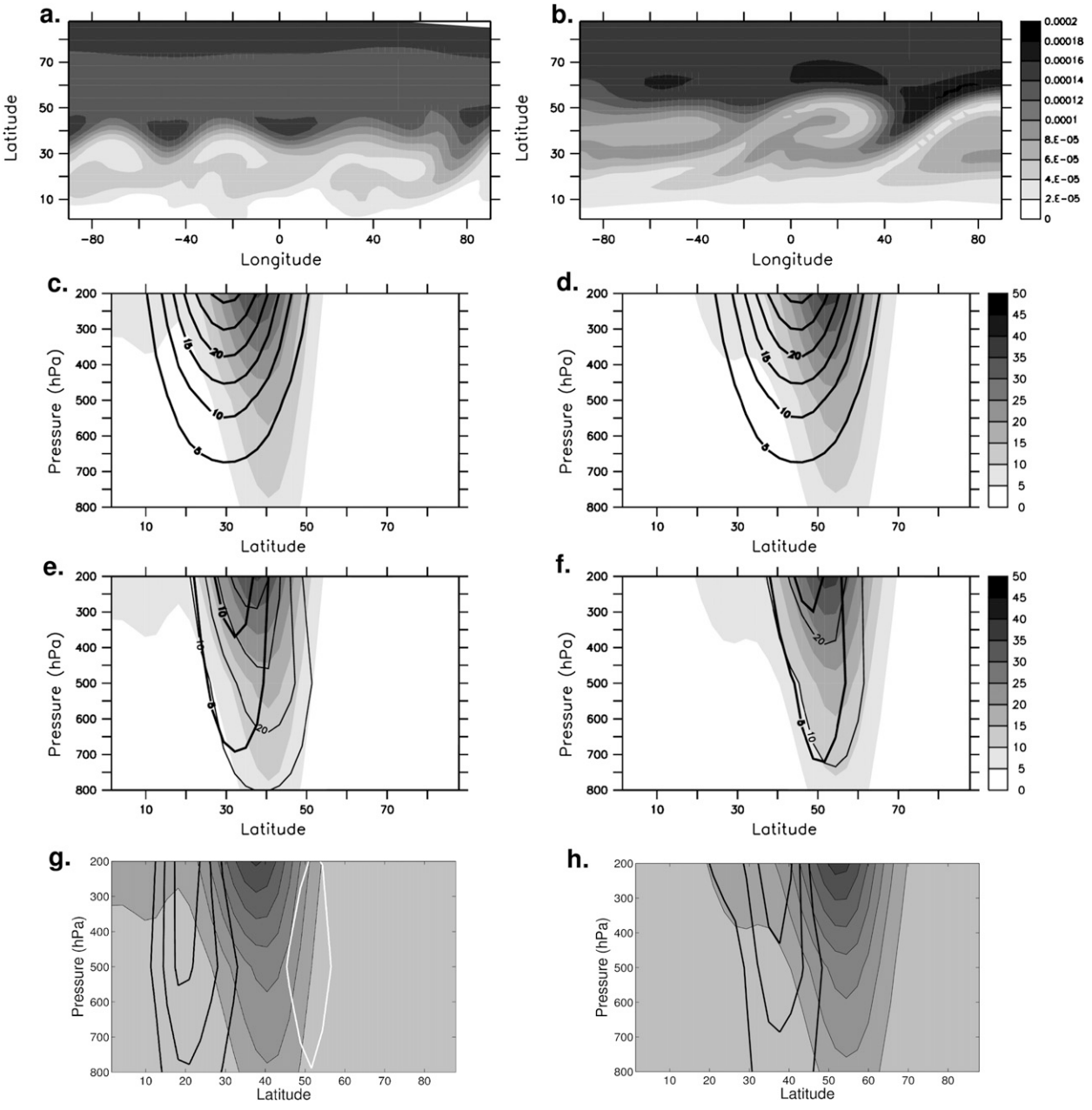

FIG. 14. Comparison between two simulations of the QG model whose restoration-baroclinicity fields are centered at (left) 30°N and (right) 45°N. (a),(b) Snapshot of absolute vorticity at 200 hPa (interval: 2×10^{-5} s^{-1}). (c),(d) Meridional cross sections of time-averaged zonally averaged zonal winds with (shading) and without (black contours) an initial perturbation (interval: 5 m s^{-1}). (e),(f) High-frequency kinetic energy (light solid contours; interval: 10 m^2 s^{-2}) and momentum fluxes (thick black contours; solid and dashed lines indicate positive and negative values, respectively; interval: 5 m^2 s^{-2}). (g),(h) Zonal average of CWB and AWB frequencies, γ_c (white contours; interval: 0.1) and γ_a (heavy black contours; interval: 0.1). Shaded areas in (e),(g) and (f),(h) are the same as in (c) and (d), respectively.

exists also in terms of eddy spatial scales. The eddy wavelength for the low-latitude simulation is smaller than for the high-latitude one, with a peak of amplitude reached for wavelengths equal to 6000 and 7000 km for the former and latter simulations, respectively (Fig. 15).

Similar simulations using the PE model show a drastic difference in the nature of the eddy feedback according to the latitude of the restoration baroclinicity. For the low-latitude case, CWB dominates (Fig. 16g), eddy momentum fluxes are negative (Fig. 16e), and the time-mean

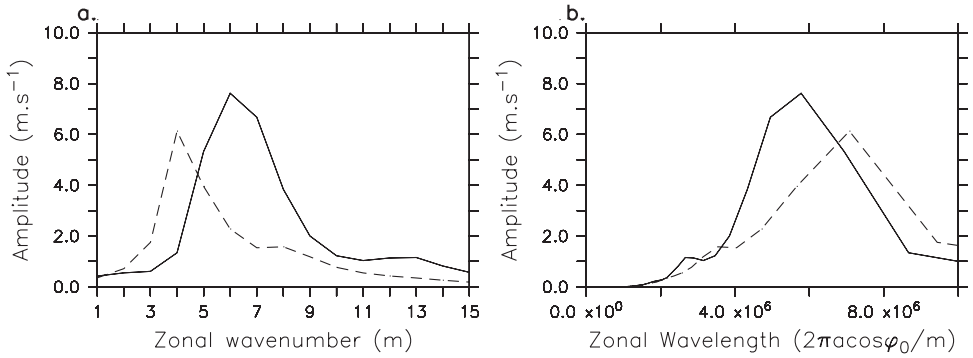

FIG. 15. Amplitude of the meridional wind as function of (a) wavenumber and (b) wavelength for restoration-baroclinicity fields centered at 30°N (solid line) and 45°N (dashed line).

jet with perturbation is southward of that without perturbation (Fig. 16c). For the high-latitude case, it is the reverse (Figs. 16d,f,h). Note also that the maximum of eddy kinetic energy is reached at 500 hPa for the former case and at 300 hPa for the latter. It supports the idea that CWB acts at lower levels than AWB. In terms of spatial length scales (Fig. 17), waves for the 30° case have usually shorter zonal wavelengths than those for the 45° case, similar to the QG simulations. The fact that shorter waves emerge more easily for lower-latitude jets than others may help to increase the positive eddy feedback because shorter waves are more able to break cyclonically.

We have noticed (not shown here) that the CWB scenario for the low-latitude restoration field may disappear by increasing the amplitude of the low-level baroclinicity whereas that of the high-latitude case leads systematically to AWB. Indeed, after a given threshold of the low-level baroclinicity, the CWB scenario shifts to an AWB scenario and the difference between the two-latitude restoration fields is much less visible. But we have checked that this transition does not exist for strong restoration forcing, that is, for much shorter restoration time scales. For example, for a restoration time scale of 3 days in the whole troposphere, the low-latitude and the high-latitude simulations systematically exhibit CWB and AWB signals, respectively, over a wide range of low-level baroclinicity amplitudes.

c. *Relaxation toward localized thermal contrasts*

1) EXPERIMENTAL DESIGN AND DIAGNOSTICS

To get localized storm tracks, we have relaxed the temperature toward nonzonally uniform fields as in FR98 and Gerber and Vallis (2007). The restoration temperature is more precisely the sum of a zonally uniform temperature and localized temperature anomalies. In contrast with similar works on the subject, the zonally uniform part is not a sine function; rather, it is linear to avoid privileging a given latitude. It is only the localized temperature anomalies that determine the latitude of maximum baroclinicity and far from these anomalies, the meridional temperature gradient is almost homogeneous (see appendix B).

Localized temperature anomalies are the sum of two monopoles of opposite signs as in FR98. Two types of localized temperature anomalies are defined: the first is composed of two monopoles centered at the same longitude (hereafter the Z case; see Fig. 19a) and the second has the negative monopole northwest of the positive monopole and is an idealized representation of the land–sea thermal contrast in winter (hereafter the NE case; see Fig. 20a). The first one is less realistic but has the advantage of simplicity because isotherms are zonal in regions of baroclinicity maximum. More details are given in appendix B.

The **E** vector introduced by Hoskins et al. (1983) and Trenberth (1986) is useful to interpret the eddy feedback onto the general circulation. In regions of divergence, the eddy feedback accelerates the zonal flow; the reverse is true in regions of convergence. We use hereafter the formulation of Trenberth (1986); the **E** vector is defined as $\mathbf{E} \equiv [(\langle \mathbf{v}'^2 - \mathbf{u}'^2 \rangle)/2, -\langle \mathbf{u}'\mathbf{v}' \rangle]$ where primes denote the high-frequency part of the flow and $\langle \cdot \rangle$ the time-mean part, and the divergence term involved in the time-mean equation is $(1/\cos\varphi)\nabla \cdot (\mathbf{E}\cos\varphi)$.

2) RESULTS

Figure 18 compares two simulations of the QG model differing in the latitude of their restoration baroclinicity but having the same shape (Z case). Both simulations lead to the strongest zonal winds at longitude 80°W, that is, in the region where the restoration baroclinicity reaches its maximum. The eddy kinetic energy is essentially localized downstream of the previous maximum (see Figs. 18c,d). In the region of maximum eddy

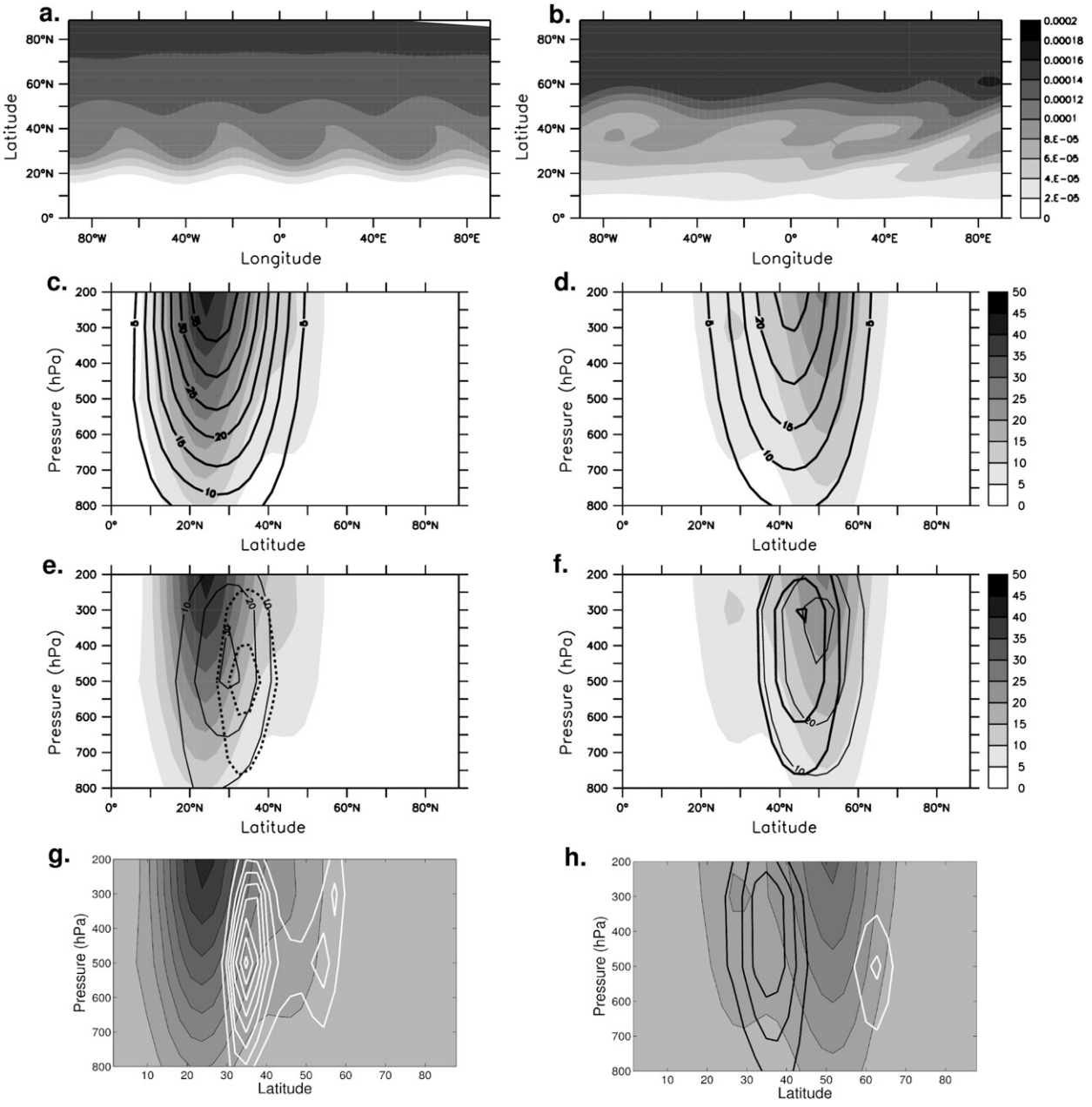

FIG. 16. As in Fig. 14, but using the PE model.

kinetic energy (more or less centered at 0°W in both simulations), a double-jet structure clearly appears. The northern jet is a continuous extension of the jet located in regions of maximum baroclinicity whereas the southern jet is not connected upstream to any jet. This picture of the climatological zonal winds reveals a succession of AWB events downstream of the maximum baroclinicity. By looking at any snapshot of these simulations (e.g., in Figs. 18c,d), most of the troughs are SW–NE tilted downstream of the baroclinicity maximum and waves propagate essentially equatorward (**E** vectors point equatorward). During AWB, an anticyclone is usually located northwest of a cyclone and westerlies are accelerated on the northern side of the anticyclone as well as on the southern side of the cyclone. This repetition of wave breaking events downstream of the baroclinicity maximum forms two regions of climatological westerlies in the same band of longitudes. Two aspects support the idea that this separation into two jets is related to the eddy feedback and AWB

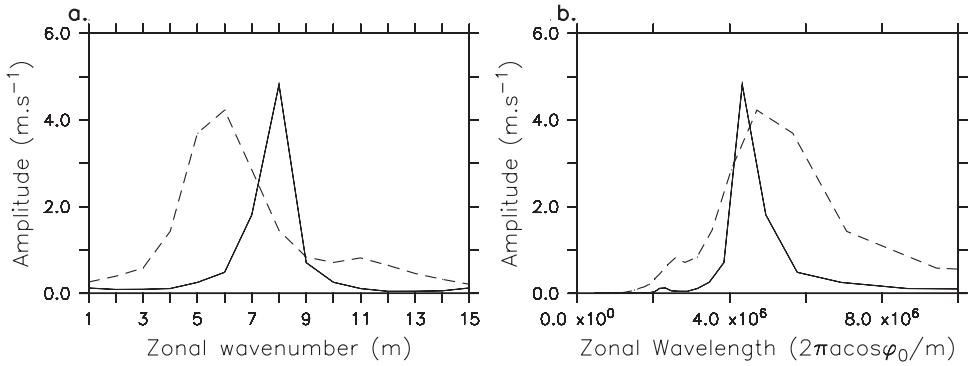

FIG. 17. As in Fig. 15, but using the PE model.

events: first, the divergence of the **E** vector is negative between the two jets and positive over the core of the northern jet (usually called the eddy-driven jet) and second, the frequency of AWB events (Figs. 18i,j) is the highest precisely between the two jets. Note that in the observations, this double-jet structure is well visible at the end of the Atlantic basin during the positive phases of the NAO when the eddy-driven Atlantic jet is pushed poleward by AWB events and separates from the subtropical African jet.

Despite close similarities between the two previous simulations, discrepancies exist. A greater jet separation appears in the high-latitude case and the eddy-driven jet as well as the climatological storm-track are strongly SW–NE oriented whereas in the low-latitude case, they are more zonal. The SW–NE orientation of the jet can be explained as follows: At the beginning of the storm-track, the eddy feedback is weak and the restoration baroclinicity is strong, with the jet being strongly related to the latter; but at the end of the storm track, the restoration baroclinicity is much weaker, eddies have stronger amplitude, and the jet is pushed poleward because of the eddy feedback. AWB events dominate in both simulations, but in the low-latitude case the frequency of occurrence of CWB is not negligible (Fig. 18i). Wave-breaking processes are thus more efficient in pushing the eddy-driven jet poleward in the high-latitude case, in accord with the conclusions in previous sections.

Numerical experiments obtained by forcing the PE model with a Z-shaped restoration field are depicted in Fig. 19. For the 45° case, the main jet is pushed poleward but less strongly than in the QG model; it has a maximum at 40°N at the longitude of maximum restoration baroclinicity (i.e., at 80°W) and extends downstream to form the eddy-driven jet for which the more northward position (50°N) is reached at longitude 20°E, where the high-frequency kinetic energy reaches its maximum (Fig. 19f). At the same longitude, a subtropical jet appears at 20°N that can be interpreted as the climatological signature of repeated SW–NE-tilted troughs propagating toward the subtropics during AWB events. It is confirmed by the high frequency of occurrence of AWB in this region (Fig. 19j), as well as by the equatorward direction taken by the E vector (Fig. 19h). For the 30° case, the scenario strongly differs from the previous one: a storm track is also present downstream of the restoration-baroclinicity maximum but its structure is NW–SE oriented and the eddy-driven jet is mainly zonal with a slight southward displacement from 80°W to 40°E (Fig. 19e). The **E** vectors have a more zonal direction and the divergence term seems to accelerate the flow more or less at the same latitude as the restoration-baroclinicity maximum (Fig. 19g). There is also a double-jet structure in the band of longitude between 60°W and 40°E, but the secondary jet is now located far north of the storm track. The presence of the latter jet may be explained by the high frequency of occurrence of CWB events (see Fig. 19i); a CWB event is usually composed of an anticyclone located northeast of a cyclone (see an example at 120°E in Fig. 19c but also in Figs. 20b and 21b), and the northern part of the anticyclone accelerates the zonal winds north of the main jet.

Similar scenarios are found by modifying the shape of the restoration field (Fig. 20) or by choosing another truncation for the model (Fig. 21). The common picture of Figs. 20 and 21 is as follows: For the low-latitude case, CWB is much more present than AWB, the eddy-driven jet is essentially zonal with sometimes a slight southward displacement, and a secondary jet appears north of the eddy-driven jet. The **E** vectors point both poleward and equatorward (see Figs. 20g and 21g), with an eddy feedback essentially maintaining the jet more or less at the same latitude as the maximum of the restoration-baroclinicity field. In contrast, for the high-latitude case, AWB dominates and the eddy-driven jet is pushed

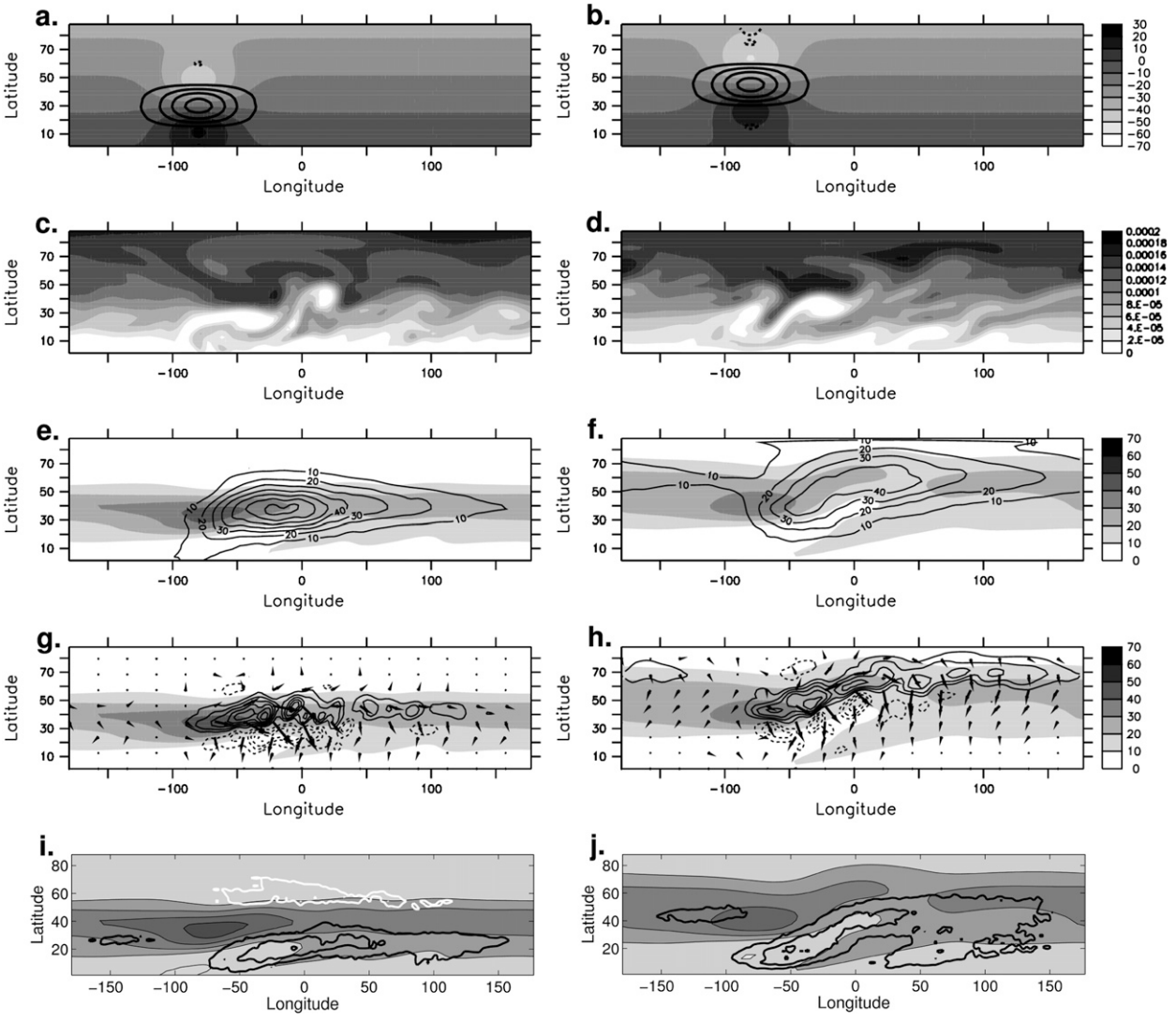

FIG. 18. Comparison between two Z-shaped simulations of the QG model whose restoration-baroclinicity fields are centered at (left) 30°N, 80°W and (right) 45°N, 80°W. (a),(b) Restoration temperature at 650 hPa (interval: 10°C) and the related baroclinicity ($R_{02}^{-1}(\partial\overline{\psi}_2|\partial y - \partial\overline{\psi}_3|\partial y)$; interval: 2×10^{-5} s^{-1}; solid and dashed lines for positive and negative values). (c),(d) Snapshot of absolute vorticity at 200 hPa (interval: 2×10^{-5} s^{-1}). (e),(f) Time-mean zonal wind (shadings; interval: 10 m s^{-1}) and high-frequency kinetic energy (black contours; interval: 10 m^2 s^{-2}) at 200 hPa. (g),(h) **E** vector and $(1/\cos\varphi)\nabla \cdot (\mathbf{E}\cos\varphi)$ (black contours; interval: 5×10^{-6} m s^{-2}) at 200 hPa. (i),(j) CWB and AWB frequencies γ_c (white contours; interval: 0.1) and γ_a (heavy black contours; interval: 0.1) at 200 hPa. Shadings in (g),(i) and (h),(j) are the same as in (e) and (f), respectively.

poleward and gets a SW–NE orientation. Furthermore, a secondary subtropical jet exists south of the former, which can be characterized as a residue of the AWB signal. The **E** vectors are southward oriented (see Figs. 20h and 21h) and their divergence is responsible for the poleward displacement of the eddy-driven jet. Some distinct behaviors between the two truncations should be outlined. For T21 simulations, storm tracks are slightly weaker and more confined longitudinally, but they were found to be more able to displace the large-scale circulation. For example, the poleward displacement in the high-latitude case is more remarkable at T21 than at T42. Part of the explanation may be the larger spatial scales of the wave breaking at T21 than at T42 (cf. Fig. 20c to Fig. 21c and Fig. 20d to Fig. 21d).

Note finally a difference in wave-breaking processes in most simulations shown previously. When AWB happens, **E** vectors are equatorward and the jet can be easily displaced poleward. However, during CWB events, **E** vectors point both poleward and equatorward, the eddy feedback is much less efficient in pushing the jet southward, and the jet takes usually a zonal direction.

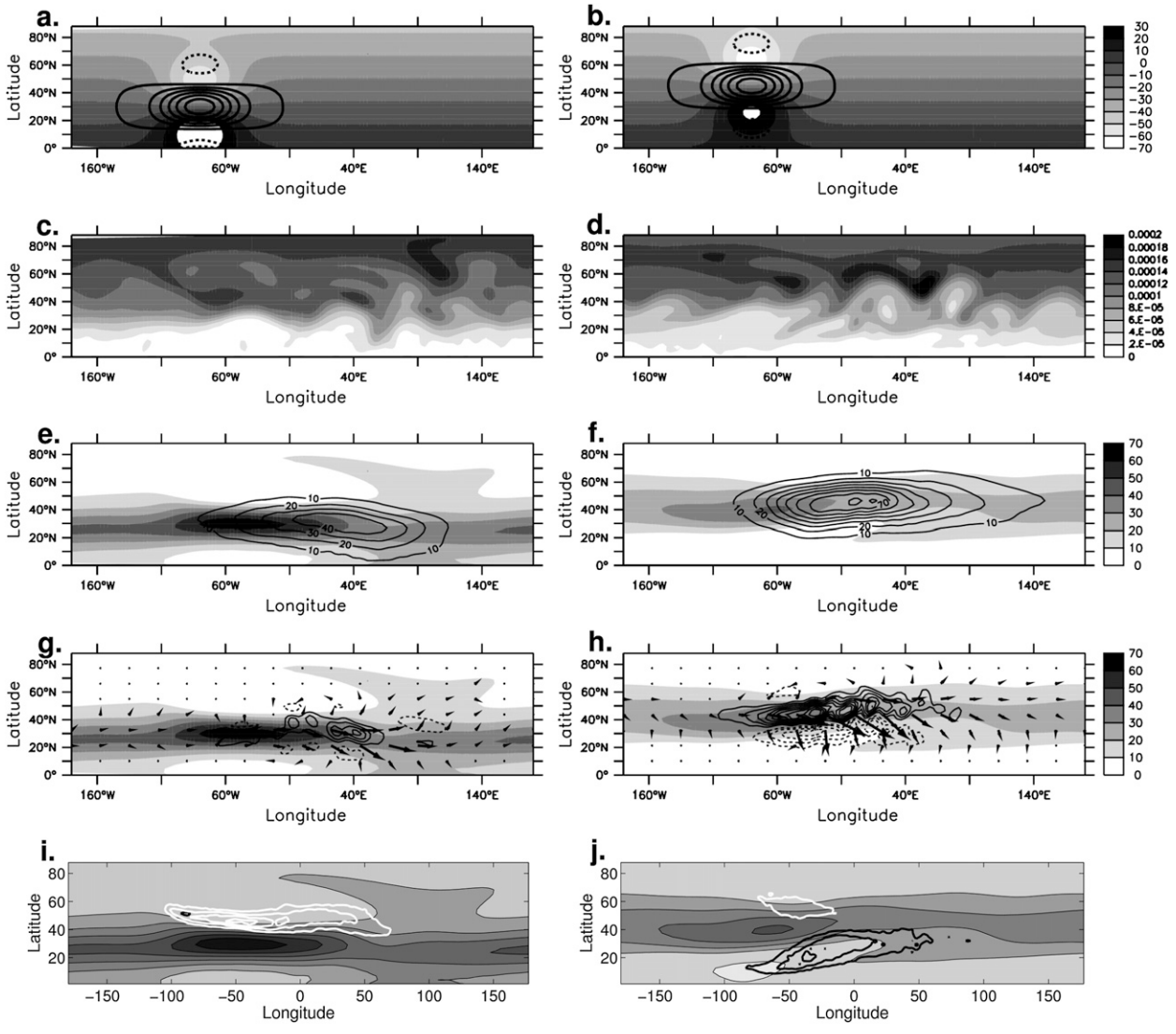

FIG. 19. As in Fig. 18, but using the PE model. In (a) and (b), the vertical level is $\sigma = 0.65$ and the baroclinicity field is approximated by the formula $(g/NT_0)\partial T/\partial y$, with $g = 10$ m s^{-2}, $N = 0.01$ s^{-1}, and $T_0 = 288$°K.

This asymmetry may be due to the fact that CWB is more effective in the low and middle levels of the troposphere and thus has less impact on the upper-level circulation.

6. Conclusions

An analysis of the PV gradient in quasigeostrophic flows on the sphere has revealed that the absolute vorticity and the stretching terms have two contradictory effects on the horizontal shape of the baroclinic waves. At upper levels, these two terms are positive around the jet core but not symmetric. Because of metric terms and the meridional derivative of f, the former increases the PV gradient and the refractive index south of the jet favoring the anticyclonic (SW–NE) tilt of upper-level waves. In contrast, because of the presence of f in its formulation, the latter is stronger on the north side of the jet and promotes the cyclonic (NW–SE) tilt of upper-level waves. At lower levels, the situation is different because the refractive index is positive in regions of negative PV gradient. The absolute vorticity gradient was shown to play a negligible role in the low-level refractive index, but the gradient of the stretching term is largely negative at lower levels and may displace the positive values of the refractive index north of the low-level jet, making it more probable that the cyclonic tilt will occur at this level. Note that the effect of the absolute vorticity gradient has been already discussed by different authors (see, e.g., section 4c of Orlanski 2003),

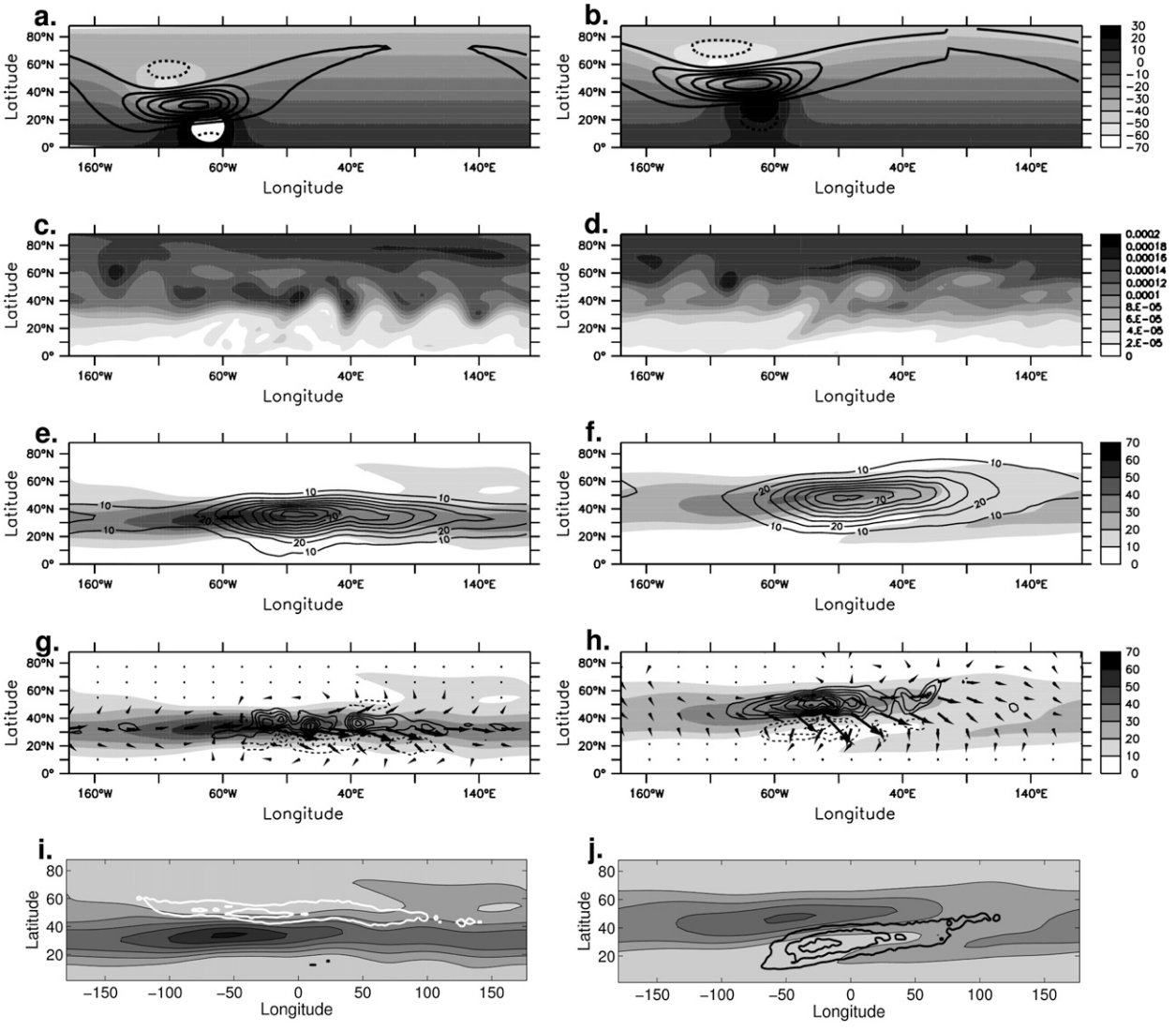

FIG. 20. As in Fig. 19, but for an NE-shaped restoration field.

but the effect of the stretching term is a new point brought out by the present study.

In the QG model of MM93, as f is replaced by a constant value f_0 in the stretching term while its full variations are taken into account in the absolute vorticity, normal modes tilt anticyclonically and AWB strongly dominates over CWB during their nonlinear evolution. The predominance of AWB was also found in the long-term simulations. In the PE model, normal modes usually exhibit a more anticyclonic tilt at upper levels and a more cyclonic tilt at lower levels, consistent with the two competing effects acting at different levels. CWB appears clearly in the nonlinear evolution of the higher-wavenumber normal modes whereas AWB is preponderant for the lower-wavenumber normal modes, as already noticed by several authors since the original work of Simmons and Hoskins (1978). This difference can be explained by the fact that normal modes for high wavenumbers are more confined at low levels than those for low wavenumbers and feel the stretching effect more than the absolute vorticity effect. Note that during the nonlinear stage, the vortex interaction mechanism of Orlanski (2003) may also help to increase this difference between high and low wavenumbers within the PE model as well as the difference of behavior between the QG and PE models.

The main purpose of the paper was to present a positive eddy feedback acting on the latitudinal variations of the zonal winds. Because the absolute vorticity and the stretching effects are respectively less and more efficient

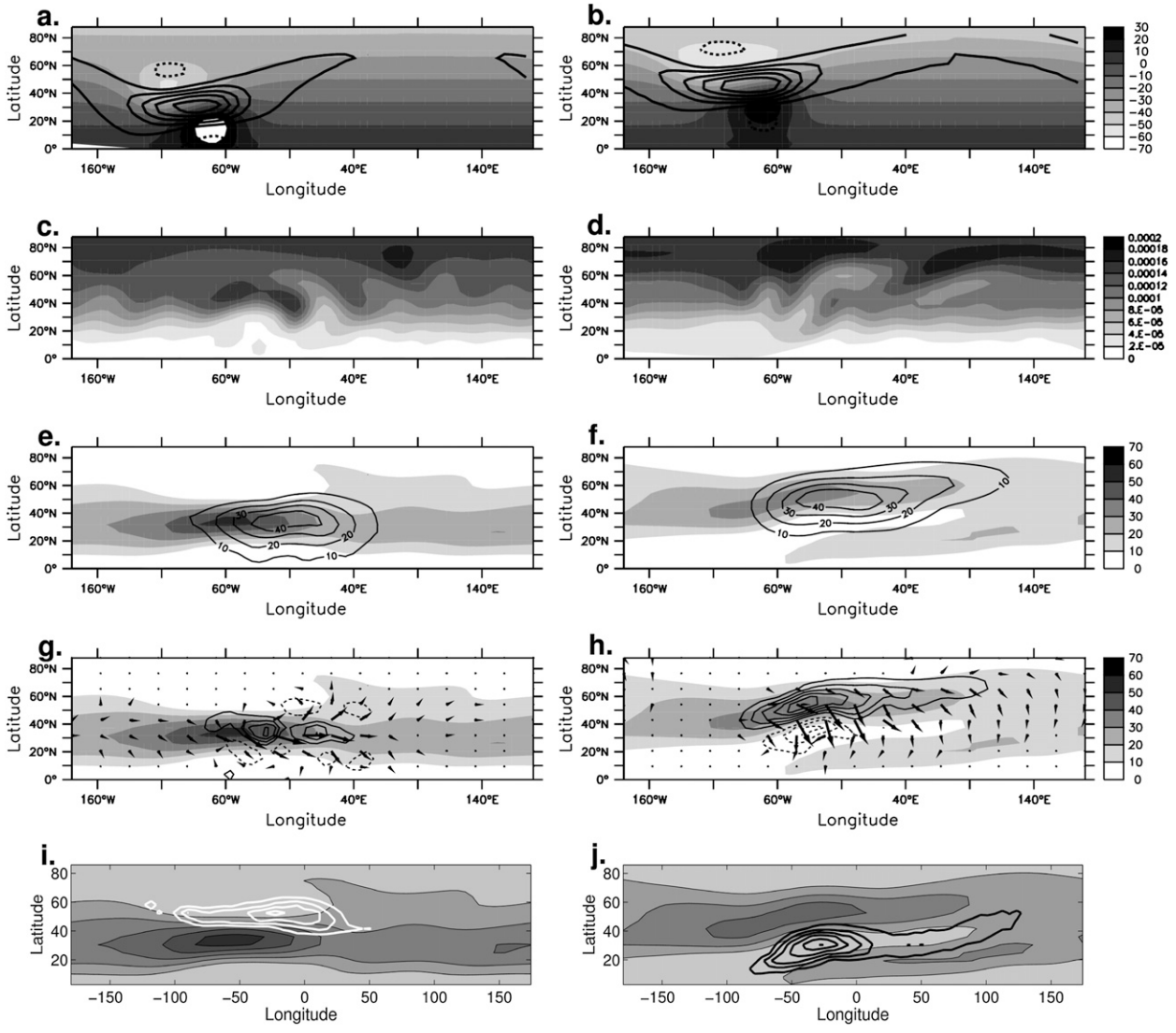

FIG. 21. As in Fig. 20, but at a T21 truncation.

as the jet latitude decreases, AWB is less probable and CWB more probable for low-latitude jets (and vice versa for high-latitude jets). This has been confirmed by the normal-mode study and the long-term integrations of both models. However, this behavior is much less visible in the QG model, which does not contain the stretching effect. These results can be interpreted as a positive feedback acting on the NAO or annular modes. In the case of the positive (negative) phase of the NAO, the jet is more northward (southward), making AWB (CWB) more probable, and thus pushing or maintaining the jet more northward (southward). Of course, the impact of the results onto the NAO should be taken with caution because the different phases of the NAO differ not only in jet latitude but also in jet asymmetries, which were not studied in the present work.

In the context of localized storm tracks, the positive eddy feedback can be perceived as follows: a more southward low-level baroclinicity supports more CWB events and the eddy-driven jet downstream of the baroclinicity maximum takes a zonal direction. Because CWB is not so efficient in pushing the upper-level jet southward, it usually maintains the jet latitude as it is at the entrance of the storm track. In contrast, a more northward baroclinicity favors AWB events, thus shifting the eddy-driven jet more poleward as they become more intense in the region of maximum eddy activity. The jet that extends from the beginning to the end of the storm track gets therefore a SW–NE orientation. We speculate that such a difference plays a role in the difference between the Pacific and Atlantic large-scale circulation in the Northern Hemisphere. The fact that

the low-level baroclinicity at the entrance of the Pacific storm track is almost 10° more southward than that in the Atlantic in winter may explain in part why the Pacific climatological jet is more zonal than the Atlantic one, which is SW–NE oriented. This speculation is supported by the frequency distribution of AWB and CWB events over the two oceanic basins: AWB is more frequent in the Atlantic than in the Pacific, and the converse is true for CWB [see Fig. 5 of Martius et al. (2007) or Fig. 2 of Strong and Magnusdottir (2008)]. It would be interesting to explore this explanation in more detail in the future by performing numerical experiments with two communicating idealized storm tracks.

APPENDIX A

Dissipative and Forcing Terms in the QG Model

The sum of the dissipative and forcing terms take the following form:

$$-D_1 + S_1 = -c_H \nabla^8 q_1' + \tau_{R1}^{-1} R_{01}^{-2} (\psi_1 - \psi_2 - \overline{\psi}_1 + \overline{\psi}_2), \tag{A1}$$

$$-D_2 + S_2 = -c_H \nabla^8 q_2' - \tau_{R1}^{-1} R_{01}^{-2} (\psi_1 - \psi_2 - \overline{\psi}_1 + \overline{\psi}_2) + \tau_{R2}^{-1} R_{02}^{-2} (\psi_2 - \psi_3 - \overline{\psi}_2 + \overline{\psi}_3), \tag{A2}$$

$$-D_3 + S_3 = -c_H \nabla^8 q_3' - \tau_E^{-1} \nabla^2 \psi_3 - \tau_{R2}^{-1} R_{02}^{-2} (\psi_2 - \psi_3 - \overline{\psi}_2 + \overline{\psi}_3), \tag{A3}$$

where q_i' denotes the PV minus the planetary vorticity and $\tau_E = 3$ days. Bars denote the restoration field; $\overline{\psi}_1 - \overline{\psi}_2$ and $\overline{\psi}_2 - \overline{\psi}_3$ are proportional to the temperature-restoration field between levels 1 and 2 and levels 2 and 3, respectively; C_H is such that the damping time scale of the shorter waves at T42 truncation is 0.1 days. In the normal-mode study, $\tau_{R1} = \tau_{R2} = 25$ days, as in the formulation of MM93, and there is of course no forcing ($S_i = 0$; $\overline{\psi}_i = 0$). In the relaxation study, $\tau_{R1} = 25$ days and $\tau_{R2} = 5$ days to get relaxation time scales similar to the PE model. Shorter time scales at lower levels characterize the usual faster heat exchange that occurs at these levels.

APPENDIX B

Restoration-Temperature Fields

The restoration-temperature field in the PE model is in large part inspired by the work of FR98. The main difference with the latter study is in the definition of the zonally symmetric part, which is linear. The restoration temperature T_E is given by

$$T_E(\lambda, \varphi, \sigma) = T_0(\sigma) + f(\sigma)\left[\Delta T_{\mathrm{ep}}\left(\frac{1}{3} - \frac{\varphi}{90}\right) + \Delta T_{\mathrm{an}} \mathrm{AN}(\lambda, \varphi)\right], \tag{B1}$$

where $\mathrm{AN}(\lambda, \varphi)$ is defined as the sum of two monopoles of opposite signs:

$$\mathrm{AN}(\lambda, \varphi) = -\sum_{i=1}^{2} (-1)^i \exp\left\{-\mathrm{coef}\left(\frac{\lambda - \lambda_i}{d\lambda_i}\right)^2 - \left[\frac{\varphi - (\varphi_0 \pm d\varphi)}{d\varphi_i}\right]^2\right\}. \tag{B2}$$

Here, $T_0(\sigma)$ is a function describing the averaged vertical temperature; it decreases from the lower to the upper troposphere with a lapse rate of -6.5 K km^{-1} starting at $T_0(1) = 288$ K. Also, $f(\sigma)$ is a sine function decreasing from 1 at $\sigma = 1$ to 0 at the tropopause (i.e., at $\sigma = 0.2$) that makes the temperature anomalies dependent on the vertical, and φ_0 is the latitude where the temperature gradient is the largest. In all experiments, $\Delta T_{\mathrm{ep}} = 70$°K and $\Delta T_{\mathrm{an}} = 50$°K. Other parameters defining the temperature anomalies are given in Table B1 for the Z case and NE case. The advantage of the Z-case formulation lies in the fact that the baroclinicity-restoration field is purely zonal and the interpretation of the results is easier. The NE case is more realistic and keeps the spatial scale of the temperature anomalies constant with latitude because the cosine of the latitude is introduced in its formula.

In the QG model, the restoration-temperature field $\overline{\psi}_i - \overline{\psi}_{i+1}$ is also the sum of a linear profile and localized temperature anomalies. The Z case is applied to the

TABLE B1. Parameter values determining the different restoration-temperature anomalies.

Parameter	Z case	NE case
λ_1	80°W	70°W
λ_2	80°W	105°W
$d\lambda_1$ for $\lambda \geq \lambda_1$	30°W	22°
$d\lambda_1$ for $\lambda < \lambda_1$	30°W	32°
$d\lambda_2$ for $\lambda \geq \lambda_2$	30°W	32°
$d\lambda_2$ for $\lambda < \lambda_2$	30°W	22°
$d\varphi$	15°	10°
$d\varphi_1$ for $\varphi \geq \varphi_1$	15°	15°
$d\varphi_1$ for $\varphi < \varphi_1$	21°	21°
$d\varphi_2$ for $\varphi \geq \varphi_2$	21°	21°
$d\varphi_2$ for $\varphi < \varphi_2$	15°	15°
coef	1	$\cos^2\varphi$

model in Fig. 18 with a ratio between the linear profile and the localized temperature anomalies slightly different from the PE model.

APPENDIX C

Wave-Breaking Detection Method

The wave-breaking detection method is inspired by the contouring approach of Strong and Magnusdottir (2008) but differs from the latter in a few aspects that are hereafter explained. The purpose of the algorithm is to detect all regions where there is a local reversal of the absolute vorticity gradient. At a given level, we consider all circumpolar contours of absolute vorticity whose values are multiples of 10^{-5} s^{-1}. As described in Strong and Magnusdottir (2008), the circumpolar contours are chosen to avoid detection of isolated patches of high or low vorticity that are not related to the wave-breaking process itself. All the contours $[\lambda(i),\varphi(i)]$ are ordered from the west to the east (i being the increment of the contour). All segments $[(\lambda(i), \varphi(i), i_i \leq i \leq i_f]$ along a contour satisfying $\lambda(i + 1) < \lambda(i) < \lambda(i - 1)$ for each i are considered to belong to a wave-breaking region. The comparison between the latitude of the first point of the segment i_i with that of the previous point along the contour $i_i - 1$ determines the nature of the wave breaking; if $\varphi(i_i - 1) \leq \varphi(i_i)\varphi(i_i - 1) \geq \varphi(i_i)$, the entire segment is considered to be a CWB (AWB) case (see Fig. C1 for an example). At each time t, we define two wave-breaking event functions $\beta_c(\lambda,\varphi,t)$ and $\beta_a(\lambda,\varphi,t)$ as follows: Initially these functions are set to zero; then for all the points belonging to the previously defined segments, we determine their closest point (λ,φ) over the initial gridpoint space. If the segment is a CWB case, $\beta_c(\lambda,\varphi,t) = 1$; if it is an AWB case, $\beta_a(\lambda,\varphi,t) = 1$. The time averages of $\beta_c(\lambda,\varphi,t)$ and $\beta_a(\lambda,\varphi,t)$ define respectively the frequencies of occurrence of CWB and AWB events and are denoted as $\gamma_c(\lambda,\varphi)$ and $\gamma_a(\lambda,\varphi)$.

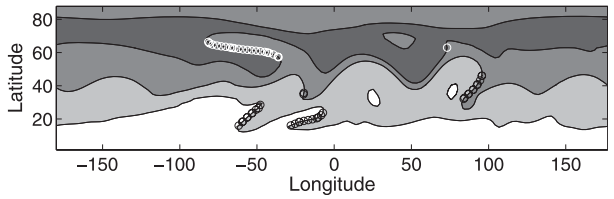

FIG. C1. Illustration of the wave-breaking detection method. The 4, 10, and 14 × 10^{-5} s^{-1} contours of absolute vorticity are represented by solid lines and shaded areas (same case as in Fig. 19d). All points belonging to a segment along a circumpolar contour detected as CWB and AWB regions are shown by open circles (white for CWB and black for AWB). See more details in the text.

REFERENCES

Akahori, K., and S. Yoden, 1997: Zonal flow vacillation and bimodality of baroclinic eddy life cycles in a simple global circulation model. *J. Atmos. Sci.,* **54,** 2349–2361.

Balasubramanian, G., and S. Garner, 1997: The role of momentum fluxes in shaping the life cycle of a baroclinic wave. *J. Atmos. Sci.,* **54,** 510–533.

Benedict, J., S. Lee, and S. Feldstein, 2004: Synoptic view of the North Atlantic Oscillation. *J. Atmos. Sci.,* **61,** 121–144.

Branstator, G., 1995: Organization of storm track anomalies by recurring low-frequency circulation anomalies. *J. Atmos. Sci.,* **52,** 207–226.

Chen, G., I. Held, and W. Robinson, 2007: Sensitivity of the latitude of the surface westerlies to surface friction. *J. Atmos. Sci.,* **64,** 2899–2915.

Fraedrich, K., E. Kirk, U. Luksh, and F. Lunkeit, 2005: The Portable University Model of the Atmosphere (PUMA): Storm track dynamics and low-frequency variability. *Meteor. Z.,* **14,** 735–745.

Frisius, T., F. Lunkeit, K. Fraedrich, and I. James, 1998: Storm-track organization and variability in a simplified atmospheric global circulation model. *Quart. J. Roy. Meteor. Soc.,* **124,** 1019–1043.

Gerber, E., and G. Vallis, 2007: Eddy–zonal flow interactions and the persistence of the zonal index. *J. Atmos. Sci.,* **64,** 3296–3311.

Hartmann, D., and P. Zuercher, 1998: Response of baroclinic life cycles to barotropic shear. *J. Atmos. Sci.,* **55,** 297–313.

Hoskins, B. J., and P. J. Valdes, 1990: On the existence of storm-tracks. *J. Atmos. Sci.,* **47,** 1854–1864.

——, I. N. James, and G. H. White, 1983: The shape, propagation, and mean-flow interaction of large-scale weather systems. *J. Atmos. Sci.,* **40,** 1595–1612.

James, I., 1994: *Introduction to Circulating Atmospheres*. Cambridge University Press, 422 pp.

Lee, S., and S. Feldstein, 1996: Two types of wave breaking in an aquaplanet GCM. *J. Atmos. Sci.,* **53,** 842–857.

Mak, M., 1991: Influences of the earth's sphericity in the quasi-geostrophic theory. *J. Meteor. Soc. Japan,* **69,** 497–511.

Marshall, J., and F. Molteni, 1993: Toward a dynamical understanding of planetary-scale flow regimes. *J. Atmos. Sci.,* **50,** 1792–1818.

Martius, O., C. Schwierz, and H. Davies, 2007: Breaking waves at the tropopause in the wintertime Northern Hemisphere: Climatological analyses of the orientation and the theoretical LC1/2 classification. *J. Atmos. Sci.,* **64,** 2576–2592.

Matsuno, T., 1970: Vertical propagation of stationary planetary waves in the winter Northern Hemisphere. *J. Atmos. Sci.,* **27,** 871–883.

Nakamura, M., and R. Plumb, 1994: The effects of flow asymmetry on the direction of Rossby wave breaking. *J. Atmos. Sci.,* **51,** 2031–2045.

Nakamura, N., 1993: Momentum flux, flow symmetry, and the nonlinear barotropic governor. *J. Atmos. Sci.,* **50,** 2159–2179.

Orlanski, I., 2003: Bifurcation in eddy life cycles: Implications for storm track variability. *J. Atmos. Sci.,* **60,** 993–1023.

——, 2005: A new look at the Pacific storm track variability: Sensitivity to tropical SSTs and to upstream seeding. *J. Atmos. Sci.,* **62,** 1367–1390.

Rivière, G., and I. Orlanski, 2007: Characteristics of the Atlantic storm-track eddy activity and its relation with the North Atlantic Oscillation. *J. Atmos. Sci.,* **64,** 241–266.

Simmons, A. J., and B. J. Hoskins, 1978: The life cycles of some nonlinear baroclinic waves. *J. Atmos. Sci.,* **35,** 414–432.

Strong, C., and G. Magnusdottir, 2008: Tropospheric Rossby wave breaking and the NAO/NAM. *J. Atmos. Sci.,* **65,** 2861–2876.

Thorncroft, C. D., B. J. Hoskins, and M. McIntyre, 1993: Two paradigms of baroclinic-wave life-cycle behaviour. *Quart. J. Roy. Meteor. Soc.,* **119,** 17–55.

Trenberth, K., 1986: An assessment of the impact of transient eddies on the zonal flow during a blocking episode using localized Eliassen–Palm flux diagnostics. *J. Atmos. Sci.,* **43,** 2070–2087.

Vallis, G., and E. Gerber, 2008: Local and hemispheric dynamics of the North Atlantic Oscillation, annular patterns and the zonal index. *Dyn. Atmos. Oceans,* **44,** 184–212.

Vautard, R., and B. Legras, 1988: On the source of midlatitude low-frequency variability. Part II: Nonlinear equilibration of weather regimes. *J. Atmos. Sci.,* **45,** 2845–2867.

Wittman, M., A. Charlton, and L. Polvani, 2007: The effect of lower stratospheric shear on baroclinic instability. *J. Atmos. Sci.,* **64,** 479–496.

Woollings, T., B. Hoskins, M. Blackburn, and P. Berrisford, 2008: A new Rossby wave–breaking interpretation of the North Atlantic oscillation. *J. Atmos. Sci.,* **65,** 609–626.